

# Redundant Actuation of Twisted and Coiled Polymer Muscles to Improve Tracking Performance

by

Ian McGinty

to obtain the degree of Master of Science  
at the Delft University of Technology,  
to be defended publicly on Wednesday August 3, 2022 at 2:00 PM.

Student number: 5293693  
Project duration: November 1, 2021 – August 3, 2022  
Thesis committee: Prof. Dr. -Ing. H. Vallery, TU Delft, chair  
Dr. ir. R. A. J. van Ostayen, TU Delft  
Prof. dr. ir. J. Hellendoorn, TU Delft  
Dr. ir. G. Smit, TU Delft

An electronic version of this thesis is available at <http://repository.tudelft.nl/>.

# Redundant Actuation of Twisted and Coiled Polymer Muscles to Improve Tracking Performance

Ian McGinty

**Abstract**—Twisted and coiled polymer muscles (TCPMs) are a type of artificial muscle with a remarkable power-to-weight ratio. However, actuation dynamics are slow compared to other artificial muscles. This work aims to improve dynamic performance by incorporating redundancy. Specifically, this work examines if TCPM bundles of heterogeneous geometries containing high-force low-bandwidth actuators and low-force high-bandwidth actuators have a substantially better tracking performance than that of bundles of homogeneous geometries. First, a white-box model was created to simulate TCPM dynamics as a function of geometric parameters. The model revealed fiber diameter is the only geometric parameter that represents a trade-off between TCPM bandwidth and maximum realizable force for isometric force tracking. Next, an optimum feedforward controller was designed to distribute the reference among redundant actuators. Finally, a brute-force optimization was conducted to find the optimum configurations of heterogeneous and homogeneous TCPM bundles and the associated tracking performances. Optimal homogeneous configurations outperformed all heterogeneous configurations irrespective of number of TCPMs in parallel or reference signal. For unidirectional configurations, a nontrivial fiber diameter optimizes tracking performance. For antagonistic configurations, tracking performance improves monotonically with increasing fiber diameter.

## NOMENCLATURE

### Fiber and Coil Geometry

$C$	Spring index
$d$	Fiber diameter
$D$	Coil diameter
$l$	Fiber length
$L_0$	Compressed coil length
$n$	TCPMs or pairs of TCPMs in parallel
$N$	Coil turns
$s_p$	Polymer chain length
$w$	Stretch ratio
$\beta_f$	Fiber bias angle
$\phi$	Angular fiber twist insertion
$\Phi$	Nondimensional twist insertion

### Electrothermal Parameters

$A_c$	Convective surface area
$c_p$	Specific heat capacity of nylon 6,6
$C_{th}$	Thermal mass of actuator
$h$	Convection coefficient
$K$	Electrothermal steady state gain
$K_{1,2,3}$	Empirically determined coefficients
$R$	Electrical resistance of heating element
$V$	Applied voltage
$T$	Actuator temperature
$T_a$	Ambient temperature

$T_{max}$	Maximum temperature of linear region
$T_{min}$	Minimum temperature of linear region
$\Delta T$	$T - T_a$
$\Delta T_s$	Incremental step in temperature
$\rho_n$	Density of nylon 6,6
$\omega_{BW}$	Electrothermal and TCPM bandwidth

### Thermomechanical Parameters

$c$	Thermal force per blocked torque
$E_i$	Untwisted Young's modulus
$\overline{E}_z$	Twisted axial Young's modulus
$F_t$	Total applied force about coil axis
$F$	Thermal force generated by blocked torque
$\overline{G}_{z\theta}$	Twisted transverse shear modulus
$G_{ij}$	Untwisted shear modulus
$S_{ij}$	Untwisted fiber stiffness matrix coefficient
$S'_{ij}$	Twisted fiber stiffness matrix coefficient
$u_i$	Assumed fiber displacement field
$z-\rho-\theta$	Fiber coordinate system
$1-2$	Polymer chain coordinate system
$\alpha_{ij}$	Untwisted thermal expansion coefficient
$\delta_\theta$	Assumed angular fiber twist per length
$\delta_z$	Assumed axial fiber expansion
$\epsilon_{ij}$	Total strain
$\epsilon_{ij}^M$	Mechanical strain
$\nu_{ij}$	Poisson's ratio
$\sigma_{ij}$	Stress
$\tau_b$	Blocked torque

### Optimal Control

$\mathbf{A}$	State matrix
$\mathbf{B}$	Input matrix
$\mathbf{F}'$	Linearized force-temperature slope
$\mathbf{F}_a$	Linearized force-temperature offset
$\Delta F_r$	Range of realizable force
$F_{min}$	Minimum force such that $T > T_{min}$
$J$	Total cost minimized by optimal control
$J_t$	Tracking cost
$J_c$	Control effort cost
$\mathbf{p}$	Costates
$r$	Offset reference such that $y - r = F - r_F$
$r_F$	Reference signal
$\mathbf{R}$	Weighting matrix
$R_0$	Weighting scalar
$\mathbf{u}$	Input vector of squared voltages
$u_{max}$	Maximum control such that $T < T_{max}$
$u_{min}$	Minimum control such that $T > T_{min}$
$y$	Output vector

## I. INTRODUCTION

### A. Motivation

Twisted and coiled polymer muscles (TCPMs) were introduced by Haines et al. in 2014 to address the current limitations of artificial muscles: large hysteresis, low work capacity, and cost [1]. Although hysteresis in large-stroke TCPM applications is not negligible [2], it is significantly smaller than comparable shape memory alloy artificial muscles [1]. The work-to-weight ratio of TCPMs can exceed 100 times that of the human bicep [1]. Radial thermal expansion and axial thermal contraction of highly-drawn polymer fibers drive thermal actuation of TCPMs [1]. Heating a twisted precursor fiber generates a torsional stroke with instantaneous speeds up to 70 000 rpm [3]. Coiling the twisted fiber and constraining both ends from rotating produces linear stroke.

This simple working principle lends itself to readily available materials and an inexpensive manufacturing process. Highly drawn polymer fibers are commercially available as fishing line or sewing thread, often made of nylon 6,6 or polyethylene<sup>1</sup>. The precursor fiber is then held under constant tension and twisted about its axis. If the number of twists inserted exceeds the critic twist number, elastic instability of the fiber results in spontaneous coil nucleation. Coils continue to form if twist is continually inserted until the entire fiber forms a helical coil, resulting in an auto-coiled TCPM. Tension of the precursor fiber dictates the ratio of coil diameter to fiber diameter, referred to as spring index. Spring indices of approximately 2 are typical of auto-coiled TCPMs [4]. Alternately, the spring index of the coil can be tuned by wrapping the twisted fiber around a mandrel before the onset of spontaneous coil nucleation. If the chirality of fiber twist and coil match, this so-called homochiral TCPM contracts when heated. If they are opposite, the heterochiral TCPM expands when heated. The coil is annealed before the mandrel is removed, resulting in a mandrel-coiled TCPM.

This work addresses a notable drawback of TCPMs: slow dynamic performance, with bandwidths on the order of 0.05 Hz in free air [5]. Other drawbacks include low efficiency on the order of 1% [1] and sensitivity to humidity [6]. This work quantifies dynamic performance as the integral of squared reference-tracking error, referred to as tracking cost. Reference signals often contain large-amplitude low-frequency components and low-amplitude high-frequency components; a square-wave reference contains components with amplitudes inversely proportional to frequency. Likewise, certain muscle geometries are better suited to producing large forces at low frequencies, and vice versa. Therefore, actuating bundles of redundant muscles of heterogeneous geometries in parallel (heterogeneous bundles) may increase performance over a specified range of frequencies compared to bundles of redundant muscles of homogeneous geometries in parallel (homogeneous bundles).

<sup>1</sup>This work specifically considers nylon 6,6 actuators because they possess superior contractile strokes and a larger operating temperature range than polyethylene actuators [1].

The Macro-Mini approach in robotics similarly uses redundancy to provide high-frequency torque with a low impedance. Zinn et al. proposed combining a high-force low-frequency series elastic actuator with a low-force high-frequency direct-drive actuator [7]. The reference signal is accordingly partitioned into low-frequency and high-frequency components before being distributed to the respective actuators [7]. This work differs from Zinn et al. in that the two or more actuators in parallel differ only in geometry. TCPM frequency range is also not pre-allocated; a multi-input single-output optimal feedforward controller is used to distribute control among TCPMs.

Contraction of heterochiral TCPMs is driven by Joule heating, while expansion is driven by convective cooling. A single unidirectional TCPM thus possesses a heating-cooling dynamic asymmetry. Symmetry is realized in an antagonistic configuration. Antagonistic configurations consist of two bundles of TCPMs of the same chirality opposing each other, or of two bundles of TCPMs of opposite chirality anchored adjacent to each other. This work considers both unidirectional configurations and geometrically-symmetric antagonistic configurations.

Both forced and natural convective cooling of TCPMs is considered in literature. Forced convective cooling requires a fan [5] [8] or heat exchanger [9] to increase the rate of TCPM cooling. Modulating the fan or heat exchanger controls the rate of convective heat transfer [8]. However, the weight, cost, and complexity of cooling equipment undermine these same principle advantages of TCPMs. Furthermore, the importance of cooling is mitigated in an antagonistic setup. Therefore, this work considers natural convection.

This work considers dynamic performance in the context of gripping applications, to which TCPMs lend themselves. Grippers are often attached to fixed multi-axis robots. TCPMs are often tethered to and powered by a fixed power source, rather than a portable battery, due to their low efficiency. Gripping tasks often involve interacting with a safety-critical or delicate environment, such as robot-human interaction or produce handling, making compliance advantageous. Like many artificial muscles, TCPMs are a form of compliant actuator. Soft grippers often engage with their environment to some constant desired force irrespective of feedback, and then later disengage. Therefore, this work investigates force-tracking performance of a square-wave reference using a predictive feedforward controller.

### B. Hypothesis

This work hypothesizes that the force-tracking performance of  $n$  TCPMs of heterogeneous geometries in parallel is substantially improved compared to that of homogeneous geometries, where a substantial improvement is defined as at least a 10% reduction tracking cost. An isometric 1 N square-wave force-tracking task is considered, such that bundle can be scaled to handle any desired application force. Thus  $n$  then represents the number of actuators employed per unit of required force, and therefore the complexity of the actuator bundle.

To validate this hypothesis, this work simulates the tracking performance of both heterogeneous and homogeneous bundles for  $n \in \{2, 3, 4\}$  unidirectional TCPMs in parallel, and for  $n = 2$  pairs of antagonistic TCPMs in parallel. Control is allocated between  $n$  redundant TCPMs via Pontryagin's minimum principle. The model is based on white-box nylon 6,6 TCPM models in literature.

### C. Report Structure

This work is organized as follows. Chapter 2 introduces a dynamic white-box model that relates geometric parameters and control input to generated force for a single TCPM. Chapter 3 proposes an optimal controller to allocate a feed-forward control signal among redundant TCPMs. Chapter 4 describes a brute-force investigation that identifies configurations of heterogeneous and homogeneous TCPM geometries that minimize tracking cost. Chapter 5 contains results, including optimum geometries and the associated simulated force responses. Chapter 6 and 7 are the discussion and conclusion, respectively.

## II. WHITE-BOX TCPM MODEL

### A. TCPM Geometric Parameters

To determine if the simulated force-tracking performance of  $n$  parallel TCPMs differs between homogeneous and heterogeneous bundles, a white-box model relating tracking performance to geometric parameters of any individual TCPM is required. Figure 1 and 2 respectively show relevant fiber and coil geometric parameters.

Twisted fiber geometry is fully characterized by fiber length  $l$ , diameter  $d$ , and nondimensional twist insertion  $\Phi$ . Twisting the fiber  $\phi$  radians results in  $\Phi = \frac{\phi d}{2l}$ . A TCPM is homochiral for  $\phi > 0$  and heterochiral for  $\phi < 0$ . TCPMs are constrained from untwisting such that  $\phi$  is constant. Fiber bias angle  $\beta_f(\rho) = \tan^{-1} \frac{\phi \rho}{l}$  is the radially-dependent angle of the polymer chain to the axis of the fiber. Characterizing twist insertion with  $\Phi$  ensures the outer fiber bias angle  $\beta_f(\rho = d/2) = \arctan \Phi$  does not scale with  $d$  or  $l$ . Note  $\beta_f$  is assumed to be temperature independent. In untwisted nylon 6,6 precursor fibers, the axial and radial thermal expansion of polymer chains can respectively be as large as  $-4\%$  [1] and  $1\%$  [10] for changes in temperature of  $200^\circ\text{C}$ . The corresponding change in  $\beta_f$  is less than  $1\%$  for  $|\beta_f| < 35^\circ$  and is considered negligible.

A fully-compressed coil of  $N$  turns at ambient temperature  $T_a$  is fully characterized by 5 geometric parameters:  $N$ ,  $l$ ,  $d$ , spring index  $C$ , and compressed coil length  $L_0$ . Two additional parameters describe a stretched coil heated to temperature  $T$ : coil diameter  $D$  and stretch ratio  $w$ . These 7 parameters are reduced to 4 independent parameters using the two trigonometric relationships shown in Figure 2 and the definition  $L_0 = Nd$ . Thus, the white-box TCPM model is a function of independent

<sup>2</sup>For a tubular fiber section of radius  $\rho$  shown in Figure 1,  $\sin \beta_f = \frac{\phi \rho}{s_p}$ , where  $s_p$  is polymer chain length. As a first order approximation,  $\frac{d\beta_f}{\beta_f} = \frac{\tan \beta_f}{\beta_f} \left( \frac{d\rho}{\rho} - \frac{ds_p}{s_p} \right)$ . This approximation ignores the shearing stresses caused by adjacent concentric tubular fiber sections.

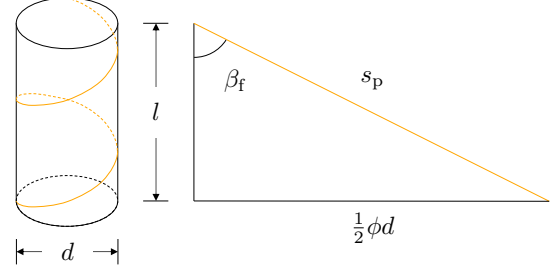


Fig. 1: Geometry of a twisted fiber of diameter  $d$  and length  $l$ . Twist insertion  $\phi$  twists highlighted polymer chain of length  $s_p$  into a helix, defined by angle  $\beta_f$  with respect to the fiber axis.

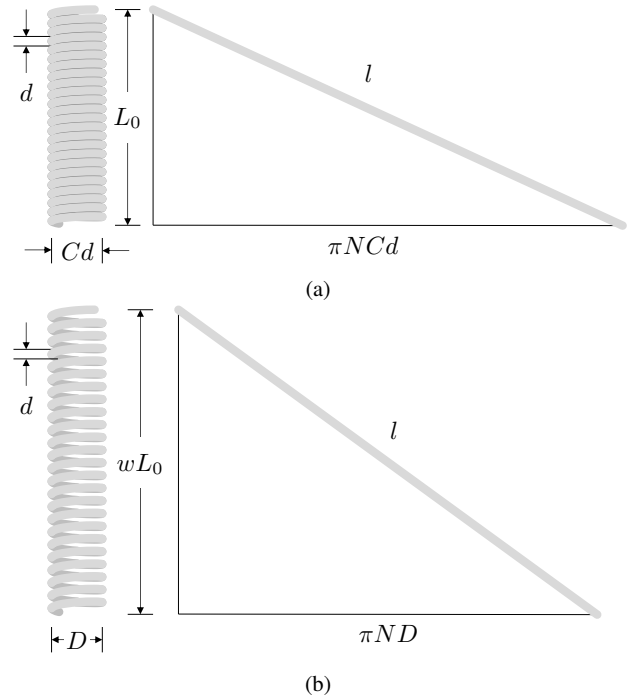


Fig. 2: (a) Coil geometric parameters at ambient temperature  $T_a$  and fully compressed length  $L_0$ . Ambient coil diameter is defined in terms of spring index  $C$ . (b) Coil geometric parameters at heated temperature  $T$  and stretched to length  $wL_0$ , where  $w$  is the stretch ratio.

fiber and coil geometric parameters  $\Phi$ ,  $d$ ,  $C$ ,  $w$ , and  $l$ . Note the temperature dependence of  $d$  and  $l$  are considered negligible when used to define coil geometry. However, the stresses induced by radial and axial thermal strains are not ignored.

### B. TCPM Modeling in Literature

White-box models in literature generally decompose the dynamic model into two submodels. The thermoelectric submodel relates applied voltage squared  $V^2$  to fiber temperature  $T$ . The thermomechanical submodel relates  $T$  to generated force axial to the coil  $F_t$  or coil length contraction  $\Delta L$ .

The electrothermal dynamics of TCPMs are often described as a first-order system in literature [5] [11] [12]. Yip and Niemeyer first proposed a linear first-order TCPM electrothermal model that only considers Joule heating and convection per Newton's law of cooling [5]. Yip and Niemeyer's linear model ignores the temperature dependence of the Joule heating element, while other authors consider resistance a linear function of temperature [13] [11]. Masuya et al. found the nonlinear effects of radiative heat transfer, thermal energy transduced into mechanical energy, and the temperature dependence of the natural convection coefficient are negligible for operating temperatures less than 120°C [14]. This work also uses Newton's law of cooling to describe TCPM dynamics. However, all TCPM literature uses grey-box techniques to determine the convective heat transfer coefficient [5] [11] [12]. Therefore other literature outside the context of TCPMs is required to analytically determine the heat transfer coefficient for white-box modeling.

Most thermomechanical dynamic models in literature attribute dynamic effects to viscous damping [5] [12] [15]. Van der Weijde et al. and Huang et al. notably account for the observed viscoelastic effects of stress relaxation and creep by employing the standard linear solid model [16] [17]. In both cases, mechanical dynamics are much slower than thermal dynamics and require system identification techniques to identify unknown parameters. For simplicity, this work ignores thermomechanical dynamic and hysteretic effects.

Static thermomechanical models are classified as either free-torsion or blocked-torque models. Both model types predict a nonlinear relationship between coil length and temperature. Thermomechanical nonlinearities were also experimentally observed by Masuya et al. [14]

Free-torsion models initially relate  $\Delta T$  to fiber untwist. If the precursor fiber is twisted, an increase in temperature drives fiber untwist [18] [19] [20] [21]. Figure 1 demonstrates how thermal expansion of fiber diameter  $d$  and thermal contraction of the wrapped polymer chain of length  $s_p$  changes fiber bias angle  $\beta_f$ . Haines et al. then relates fiber untwist to coil length contraction  $\Delta L$  using Love's helix equation [1], a purely geometric relationship. This implementation predicts length contraction independent of elastic material properties. It has been validated on nylon TCPMs for temperatures up to 120°C and outer fiber bias angles of 24° [1].

Blocked-torque models initially determined the reaction torque, or blocked torque  $\tau_b$ , associated with an increase in temperature  $\Delta T$  assuming the fiber is constrained from untwisting. Yang and Li first relate  $\Delta T$  to blocked torque  $\tau_b$  via shear stresses  $\sigma_{z\theta}$  [22], therefore incorporating elastic material properties. Tang et al. further simplified this relationship by assuming certain stress and strain contributions were negligible based on observations from finite element analysis [10]. Castigliano's method then relates blocked torque applied about the axis of the fiber to both coil length contraction  $\Delta L$  and applied force about the axis of the coil  $F_t$  [22] [10]. Tang et al. validated this model on nylon TCPMs for temperatures up to 180°C and fiber bias angles of 44° [10]. This model is validated for a larger range of temperature and twist insertion than any other model in literature. As a blocked-torque model,

it incorporates elastic material properties. Tang et al. also experimentally determine more transverse isotropic nylon 6,6 material properties for use in their model than any other work. This work accordingly models TCPM thermomechanics using the Tang et al. model.

### C. Electrothermal Model

Applied voltage  $V$  drives an increase in actuator temperature  $\Delta T = T - T_a$  due to Joule heating. The electrothermal dynamics are described via Newton's law of cooling:

$$C_{th}\dot{T} = \frac{V^2}{R} - hA_c\Delta T, \quad (1)$$

where  $C_{th}$  is the actuator thermal mass,  $R$  is the actuator electrical resistance,  $h$  is the convection coefficient, and  $A_c$  is the actuator convective surface area. This model assumes fiber and heating element temperature are identical and homogeneous throughout the actuator. It also takes the lumped mass assumption where conduction is negligible compared to convection, which is valid for Biot numbers less than 0.1.

Fiber properties  $C_{th}$  and  $A_c$  can be expressed in terms of fiber diameter  $d$  and fiber length  $l$ . Assuming the thermal mass of the heating element is negligible compared to that of the fiber,  $C_{th} = c_p\rho_n\frac{\pi}{4}d^2l$ , where  $c_p$  and  $\rho_n$  are respectively the specific heat capacity and density of nylon 6,6. Ignoring the surface area contribution of the heating element and the ends of the nylon fiber,  $A_c = \pi dl$ .

Similarly, convective coefficient  $h$  can be expressed in terms of the coil geometric parameters: fiber diameter  $d$ , spring index  $C$ , stretch ratio  $w$ , and fiber length  $l$ . Hauser experimentally determined natural convective coefficients for horizontal coils as a function  $d$ ,  $C$ , and  $w$ . [23]. Hauser relates convection coefficient  $h$  to geometric properties  $d$ ,  $C$ , and  $w$  and the thermophysical properties of air [23]:

$$h = \frac{\lambda w}{d\pi C}K_1, \quad (2)$$

where  $\lambda$  is the thermal conductivity of air. Empirically determined coefficients  $K_1$ ,  $K_2$ , and  $K_3$  are functions of standard gravity  $g$  and the thermal expansion coefficient  $\beta$ , Prandtl number  $Pr$ , and kinematic viscosity  $\nu$  of air<sup>3</sup> [23]:

$$\begin{aligned} K_1 &= (1.3248 + 0.0343K_2 + 0.0029K_2^2 - 0.00003K_2^4)^{K_2}, \\ K_2 &= \log_{10} g + \log_{10} \frac{\beta Pr \Delta T}{\nu^2} + 3 \log_{10} K_3, \\ K_3 &= d \left( 1 + \frac{\pi C - 1}{w} \right). \end{aligned}$$

Equation 2 is valid for  $-6 < K_2 < 4$ . The third term of  $K_2$  is a function of coil geometry, while the second term of  $K_2$  and  $\lambda$  in Equation 2 are temperature dependent. For anticipated operating range  $T_{min} = 110^\circ\text{C}$  and  $T_{max} = 160^\circ\text{C}$  (see Subsection II-F), variation in  $K_2$  over the range of operating temperatures is less than 1% compared to variation in  $K_2$  due to anticipated range of geometries. Temperature

<sup>3</sup>Per [23],  $\beta$  is evaluated at  $T_a + \Delta T$ , while  $\lambda$ ,  $Pr$ , and  $\nu$  are evaluated at  $T_a + \frac{1}{2}\Delta T$ .

dependence of  $K_2$  is thus ignored. If  $\lambda(\Delta T)$  is approximated as  $\lambda(\Delta T = \frac{1}{2}T_{\max} + \frac{1}{2}T_{\min})$ , resulting in less than 5% error, convection coefficient  $h$  is independent of temperature.

The Laplace transform of Equation 1 in terms of fiber and coil geometric parameters is:

$$\frac{\Delta T(s)}{V^2(s)} = \frac{K}{s/\omega_{\text{BW}} + 1}, \quad (3)$$

where steady state gain

$$K = \frac{1}{R\lambda} \frac{C}{wK_1 l} \quad (4)$$

and bandwidth

$$\omega_{\text{BW}} = \frac{4\lambda}{\pi\rho_n c_p} \frac{wK_1}{Cd^2}. \quad (5)$$

Note  $\lambda$  and  $K_1$  are assumed to be temperature-independent. Equation 3 is then independent of temperature if Joule heating element resistance  $R$  is also assumed to be temperature independent. Therefore, a constantan heating element is used, which has a resistivity temperature coefficient of  $2 \times 10^{-5} \text{ K}^{-1}$  [24].

Operating temperature must be kept between  $T_{\min}$  and  $T_{\max}$ , as discussed in Section II-F. This is physically realized via input saturation. To enforce these operating conditions across all input frequencies,  $V^2$  is conservatively constrained such that  $KV^2 \in [T_{\min}, T_{\max}]$ .

#### D. Fiber Thermomechanical Model

If the temperature of a twisted precursor fiber constrained from rotating about its axis is elevated  $\Delta T$  above the environmental temperature  $T_a$ , then the fiber produces a counteracting blocked torque  $\tau_b$ . This torque is a function of fiber diameter  $d$  and twist insertion  $\phi$ .

Twist insertion rotates the material properties of a straight fiber by angle  $\beta_f$ , defined with respect to the axis of the fiber (see Figure 3). Note  $\beta_f$  within the fiber is radially dependent:  $\tan \beta_f(\rho) = \frac{\phi\rho}{l}$ . Highly drawn untwisted nylon 6,6 fibers possess transverse isotropic material properties with untwisted stiffness matrix [25]

$$\mathbf{S} = \begin{bmatrix} \frac{1}{E_1} & -\frac{\nu_{12}}{E_1} & -\frac{\nu_{12}}{E_1} & 0 & 0 & 0 \\ -\frac{\nu_{12}}{E_1} & \frac{1}{E_2} & -\frac{\nu_{23}}{E_2} & 0 & 0 & 0 \\ -\frac{\nu_{12}}{E_1} & -\frac{\nu_{23}}{E_2} & \frac{1}{E_2} & 0 & 0 & 0 \\ 0 & 0 & 0 & \frac{2+2\nu_{23}}{E_2} & 0 & 0 \\ 0 & 0 & 0 & 0 & \frac{1}{G_{12}} & 0 \\ 0 & 0 & 0 & 0 & 0 & \frac{1}{G_{12}} \end{bmatrix}^{-1}, \quad (6)$$

where  $E_1$  and  $E_2$  are Young's moduli,  $G_{23}$  is the transverse shear modulus,  $\nu_{12}$  and  $\nu_{23}$  are Poisson's ratios, and subscripts 1 and 2 respectively denote untwisted axial and radial component axes in Figure 3 (a). Rotating the elastic material properties  $\beta_f$  from the 1–2 coordinate system to the  $z$ – $\rho$ – $\theta$  coordinate system in Figure 3 (b) results in a radially-dependent twisted stiffness matrix  $\mathbf{S}' = \mathbf{PSP}^T$ , where rotation matrix [26]

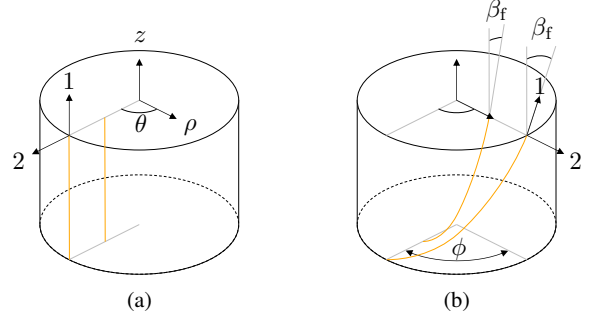


Fig. 3: A fiber in the (a) untwisted and (b) twisted state. Individual polymer chains at radii  $d/2$  and  $d/4$  are highlighted for clarity. Twisting the fiber  $\phi$  radians rotates precursor material properties by radially-dependent fiber bias angle  $\beta_f(\rho)$ . To obtain radially-dependent material properties of the twisted fiber, precursor-fiber properties in the 1–2 coordinate system are rotated to the  $z$ – $\rho$ – $\theta$  fiber coordinate system.

$$\mathbf{P} = \begin{bmatrix} c_\beta^2 & s_\beta^2 & 0 & 0 & 0 & 2c_\beta s_\beta \\ s_\beta^2 & c_\beta^2 & 0 & 0 & 0 & -2c_\beta s_\beta \\ 0 & 0 & 1 & 0 & 0 & 0 \\ 0 & 0 & 0 & c_\beta & s_\beta & 0 \\ 0 & 0 & 0 & -s_\beta & c_\beta & 0 \\ -c_\beta s_\beta & c_\beta s_\beta & 0 & 0 & 0 & c_\beta^2 - s_\beta^2 \end{bmatrix}, \quad (7)$$

$c_\beta$  denotes  $\cos \beta_f$ , and  $s_\beta$  denotes  $\sin \beta_f$ . Similarly rotating thermal expansion coefficients  $\alpha_i$  results in [26]

$$\alpha_z = \alpha_1 \cos^2 \beta_f + \alpha_2 \sin^2 \beta_f, \quad (8)$$

$$\alpha_\theta = \alpha_1 \sin^2 \beta_f + \alpha_2 \cos^2 \beta_f, \quad (9)$$

$$\alpha_\rho = \alpha_2, \quad (10)$$

$$\alpha_{z\theta} = 2(\alpha_2 - \alpha_1) \cos \beta_f \sin \beta_f, \quad (11)$$

where subscripts  $z$ ,  $\rho$ , and  $\theta$  denote twisted properties defined per the coordinate system in Figure 3. Axial thermal expansion coefficient  $\alpha_1$  is negative while radial thermal expansion coefficient  $\alpha_2$  is positive for nylon 6,6. Note that  $\alpha_{z\theta} \neq 0$  for  $\beta_f \neq 0$  such that twist insertion results in some nonzero shear thermal expansion coefficient  $\alpha_{z\theta}$ . Accordingly, a change in temperature  $\Delta T$  generates a blocked torque  $\tau_b$  if the fiber is constrained from rotating.

Blocked torque is computed by decomposing the fiber core into tubular layers of a finite thickness  $\Delta\rho$ . Stiffness matrix coefficients  $S'_{ij}$  and thermal expansion coefficients  $\alpha_i$  are defined based on the bias angle of the layer. The following radially-dependent displacement field is imposed on each layer [22]:

$$(u_\rho \quad u_\theta \quad u_z) = (u_\rho(\rho) \quad \delta_\theta \rho z \quad \delta_z z). \quad (12)$$

Infinitesimal strain theory relates displacements per Equation 12 to mechanical strains  $\epsilon^M$ . Constitutive relationships equate stress and mechanical strain via the stiffness matrix. A suf-

ficiently small step in temperature<sup>4</sup>  $\Delta T_s$  drives increment in stress [22]:

$$\Delta\sigma_{z\theta}(\rho, T) = S'_{16}\epsilon_z^M + S'_{26}\epsilon_\theta^M + S'_{36}\epsilon_r^M + S'_{66}\epsilon_{z\theta}^M \quad (13)$$

$$= S'_{16}(\epsilon_z - \alpha_z\Delta T_s) + S'_{26}(\epsilon_\theta - \alpha_\theta\Delta T_s) + S'_{36}(\epsilon_r - \alpha_r\Delta T_s) + S'_{66}(\epsilon_{z\theta} - \alpha_{z\theta}\Delta T_s), \quad (14)$$

where  $\epsilon$  denotes total strain, and  $S'_{ij}$  and  $\alpha_i$  are temperature dependent. Tang et al. proposed two simplifications to Equation 14. First, the fiber was allowed to axially expand or contract while still being constrained from rotating ( $\delta_\theta = 0$ ), resulting in strains  $\epsilon_z = \delta_z$  and  $\epsilon_{z\theta} = \delta_\theta\rho = 0$ . Second, a finite element analysis investigating internal strains of a twisted fiber revealed that circumferential strain  $\epsilon_\theta$  and the contribution of radial mechanical strain to shearing stress  $S'_{36}\epsilon_r^M$  are negligible [10]. Equation 14 is then

$$\Delta\sigma_{z\theta} = S'_{16}(\Delta\delta_z - \alpha_z\Delta T_s) - S'_{26}\alpha_\theta\Delta T_s - S'_{66}\alpha_{z\theta}\Delta T_s, \quad (15)$$

where  $\Delta\delta_z$  is determined by assuming no axial force is applied to fiber such that the integral of the axial stress over the fiber cross section is zero ( $\bar{\sigma}_z = 0$ ) [10]:

$$\Delta\delta_z = \frac{\sum_{\rho=0}^{d/2} (S'_{11}\alpha_z + S'_{12}\alpha_\theta + S'_{16}\alpha_{z\theta})\pi\rho\Delta\rho}{\sum_{\rho=0}^{d/2} S'_{11}\pi\rho\Delta\rho}\Delta T_s. \quad (16)$$

Blocked torque is determined by taking the summation of the incremental moment induced by shear stress  $\Delta\sigma_{z\theta}(\rho, T)\rho$  across the fiber cross section and from temperature  $T_a$  to  $T$ . As  $\Delta\rho \rightarrow 0$  and  $\Delta T_s \rightarrow 0$ , the summation becomes [22]

$$\tau_b = 2\pi \int_{T_a}^T \int_0^{d/2} \frac{d\sigma_{z\theta}(\rho, T)}{dT} \rho^2 d\rho dT. \quad (17)$$

### E. Coil Thermomechanical Model

A blocked torque  $\tau_b$  applied about the axis of a coiled fiber drives coil length contraction  $\Delta L$  as a function of total applied load about the axis of the coil  $F_t$ , where  $\Delta L$  is change in length from fully-compressed coil length  $L_0$  at ambient temperature (see Figure 4). Castigliano's method predicts  $\Delta L$  is linear with applied load  $F_t$  and blocked torque  $\tau_b$  [22] [10]:

$$\Delta L = f_1 F_t - f_2 \tau_b, \quad (18)$$

where  $f_1$  and  $f_2$  are nonlinear functions of coil geometric parameters. Experimental observations confirm TCPM thermal contraction  $f_2\tau_b$  is independent of applied load  $F_t$  [1] [4] [10]. Independent of  $\Delta L$ , the force generated by blocked torque is  $F = \frac{f_2}{f_1}\tau_b = c\tau_b$ , where thermal constant

$$c = \left[ \frac{d}{2\pi\sqrt{\gamma}} \left( \gamma + \left( \frac{2\overline{G}_{z\theta}}{\overline{E}_z} - 1 \right) w^2 \right) + \frac{\pi d}{4\sqrt{\gamma}(\gamma - w^2)} \left( \gamma + \left( \frac{\overline{G}_{z\theta}}{\overline{E}_z} - 1 \right) w^2 \right) \right]^{-1}. \quad (19)$$

<sup>4</sup>Step in temperature  $\Delta T_s$  should not be confused with the difference in actuator temperature  $T$  and ambient temperature  $T_a$ ,  $\Delta T$ .

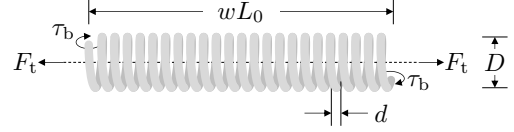


Fig. 4: A TCPM of  $N$  turns and a total applied axial force of  $F_t$ . If the fiber is constrained from untwisting, temperature-dependent blocked torque  $\tau_b$  drives coil length contraction.

Note that  $\gamma = \pi^2 C^2 + 1$ , and that  $\overline{E}_z$  and  $\overline{G}_{z\theta}$  are the average axial Young's modulus and transverse shear modulus over the cross section of the twisted fiber<sup>5</sup>. Equation 19 accounts for strain energies from torsion induced by  $\tau_b$ , and the axial loading, bending, torsion, and shear caused by  $F_t$  about the coil axis. Thus, this nonlinear relationship is valid for large deflections. Coil curvature effects present for low coil indices are ignored [28].

This implementation of Castigliano's method in conjunction with the blocked-torque model from Subsection II-D closely agrees with experimental testing in literature. Tang et al. validated this model for an auto-coiled nylon 6,6 TCPM with a spring index less than 2 for temperatures up to 180°C [10]. To confirm this work correctly numerically implements this thermomechanical model, this work exactly reproduced the analytical results of Tang et al.

### F. Model Linearization

Figure 5 shows the complete nonlinear TCPM model used to simulate performance. Model parameters include  $K$ ,  $\omega_{BW}$ ,  $\tau_b$ , and  $c$ . Bandwidth  $\omega_{BW}$  is independent of nondimensional fiber twist  $\Phi$  and fiber length  $l$ , thus  $\Phi$  and  $l$  affect the steady state force generated per input  $V^2$  without influencing dynamics. Because input saturation constrains realizable steady state actuator temperature such that  $KV^2 \in [T_{\min}, T_{\max}]$ , the thermal forces  $F$  is independent of  $l$ . Note  $l$  also affects TCPM stiffness and thus contraction  $\Delta L$ , when not loaded isometrically. The nonlinear dependence of blocked torque  $\tau_b$  on temperature  $T$  (and thus the nonlinearity of the model) is driven by both temperature-dependent material properties, and the nonlinear relationship between material properties and blocked torque.

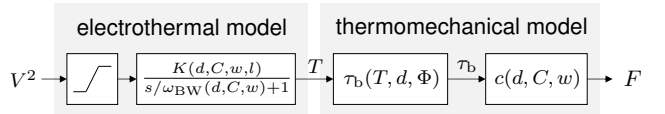


Fig. 5: A block diagram of the nonlinear first-order TCPM model, partitioned into the electrothermal and thermomechanical submodels. Model parameters  $K$ ,  $\omega_{BW}$ ,  $\tau_b$ , and  $c$  are functions of geometric parameters  $d$ ,  $C$ ,  $w$ ,  $l$ , and  $\Phi$ .

<sup>5</sup>Elastic moduli  $\overline{E}_z$  and  $\overline{G}_{z\theta}$  depend on both temperature and twist insertion. However, for  $\gamma \gg w^2$ , the temperature and twist dependent of ratio  $\overline{E}_z/\overline{G}_{z\theta}$  is negligible such that both  $\overline{E}_z$  and  $\overline{G}_{z\theta}$  are taken as constants. [27] provides a method for computing  $\overline{E}_z$  and  $\overline{G}_{z\theta}$  as functions of temperature and twist insertion.

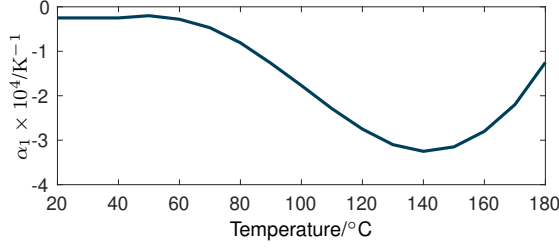


Fig. 6: Axial thermal expansion coefficient  $\alpha_1$  of a 0.5 mm diameter nylon 6,6 fiber as a function of temperature, as experimentally determined by Tang et al. [10] Expansion coefficient between 20°C and 40°C is assumed constant.

TABLE I: Elastic moduli [10], Poisson’s ratios [29], and radial thermal expansion coefficient [1] used in this work and used by [10]. Elastic moduli are of a 0.5 mm diameter nylon 6,6 fiber as measured by [10]. Twisted elastic moduli correspond to an outer fiber bias angle of 44° ( $\Phi = 0.96$ ).

$\frac{E_1}{\text{GPa}}$	$\frac{E_2}{\text{GPa}}$	$\frac{G_{23}}{\text{GPa}}$	$\nu_{12}$	$\nu_{23}$	$\frac{\bar{E}_z}{\text{GPa}}$	$\frac{\bar{G}_{z\theta}}{\text{GPa}}$	$\frac{\alpha_2}{\text{K}^{-1}}$
2.66	0.56	1.13	0.48	0.26	2.2	0.43	$8.1 \cdot 10^{-5}$

This work uses material properties used by Tang et al. Their implementation of an identical thermomechanical model is validated for the largest temperature range in literature, and closely agrees with experimental results [10]. Tang et al. experimentally determined axial thermal expansion coefficient as a function of temperature, shown in Figure 6. All other material properties are approximated as temperature independent and shown in Table I.

Blocked torque is approximately linear with temperature for 110°C to 160°C (see Figure 7) using the material properties shown in Figure 6 and Table I. The blocked torque generated at 110°C is small compared to that compared that at 160°C. Above 160°C the TCPMs are at risk of melting. TCPMs are thus constrained to only operate in the approximately linear region, realized via input constraints. Replacing the nonlinear  $\tau_b$  block in Figure 5 with a linear approximation between  $T_{\min} = 110^\circ\text{C}$  and  $T_{\max} = 160^\circ\text{C}$  results in a linear first-order TCPM model.

### III. OPTIMAL CONTROL

#### A. Linear Model of Multiple TCPMs

The linear model proposed in Subsection II-F is used to construct an optimal controller which allocates control among redundant TCPMs. A linear fit is applied to the thermomechanical model for temperature range  $\Delta T_i \in [T_{\min} - T_a, T_{\max} - T_a]$  for each individual TCPM  $i$ . Thermal force as a function of temperature for TCPM  $i$  is thus approximated as

$$F_i \approx F'_i \Delta T_i + F_{a_i}. \quad (20)$$

Note that force offset  $F_{a_i}$  corresponds to thermal force if the linear fit is extended to ambient temperature  $T_a$  such that  $\Delta T_i = 0$ , and represents a physically unrealizable force.

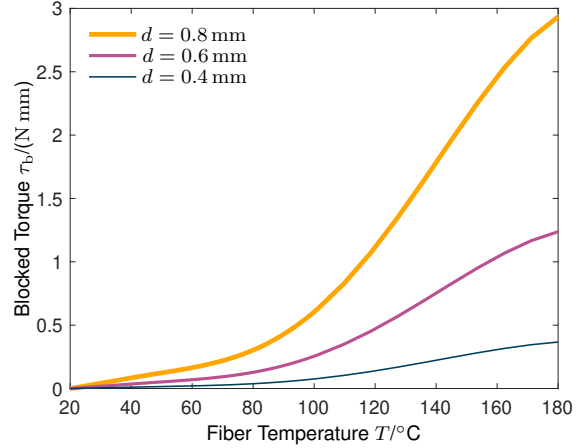


Fig. 7: Blocked torque as a function of temperature for various fiber diameters  $d$  with a constant outer fiber bias angle of 35° ( $\Phi = 0.70$ ). The region between 110°C and 160°C is approximately linear.

The state space representation of  $n$  unidirectional TCPMs in parallel is

$$\dot{\mathbf{T}} = \mathbf{A}\Delta\mathbf{T} + \mathbf{B}\mathbf{u} \quad (21)$$

$$\mathbf{y} = \mathbf{F}'^T \Delta\mathbf{T} \quad (22)$$

where  $\mathbf{A}$  and  $\mathbf{B}$  are  $n \times n$  diagonal matrices such that  $A_{ii} = -\omega_{\text{BW}_i}$  and  $B_{ii} = \omega_{\text{BW}_i} K_i$ ,  $\mathbf{u}$  is an  $n \times 1$  vector of control inputs, and total thermal force produced by  $n$  TCPMs is  $F \approx \mathbf{y} + \sum \mathbf{F}_a$ . The state space representation of  $n$  pairs of symmetrically-antagonistic TCPMs in parallel consists of a  $2n$ -dimensional system. Diagonal state and output matrices thus repeat such that  $A_{kk} = A_{ii} = -\omega_{\text{BW}_i}$  and  $B_{kk} = B_{ii} = \omega_{\text{BW}_i} K_i$  where  $k = 2i$ . Similarly, for the  $2n \times 1$  output matrix  $F'_k = -F'_i$ , and for the linear offset  $F_{ak} = -F_{ai}$  such that  $\sum \mathbf{F}_a = 0$ .

#### B. Pontryagin’s Minimum Principle

A logical cost function to optimally distribute control between  $n$  TCPMs weighs both  $J_t$ , squared tracking error between thermal force  $F$  and force reference  $r_F$ , and the weighted control effort  $J_c$ :

$$J = J_t + J_c = \frac{1}{2} \int_{t_0}^{t_f} (y - r)^2 + \mathbf{u}^T \mathbf{R} \mathbf{u} dt, \quad (23)$$

where reference  $r = r_F + \sum \mathbf{F}_a$  such that  $y - r = F - r_F$ , and  $n \times n$  diagonal matrix  $\mathbf{R}$  weighs control effort. The corresponding Hamiltonian is a function of states  $\Delta\mathbf{T}$  and costates  $\mathbf{p}$ :

$$\mathcal{H}(\Delta\mathbf{T}, \mathbf{u}, \mathbf{p}, t) = \frac{1}{2} y^2 - r y + \frac{1}{2} r^2 + \frac{1}{2} \mathbf{u}^T \mathbf{R} \mathbf{u} + \mathbf{p}^T (\mathbf{A}\Delta\mathbf{T} + \mathbf{B}\mathbf{u}). \quad (24)$$

Because of input constraints  $\mathbf{u} \in [\mathbf{u}_{\min}, \mathbf{u}_{\max}]$ , the Riccati equation cannot be employed. Therefore Pontryagin's minimum principle is used to solve for optimal control  $\mathbf{u}^*$ , states  $\Delta\mathbf{T}^*$ , and costates  $\mathbf{p}^*$  that minimize cost  $J$ :

$$\dot{\mathbf{T}}^* = \frac{\partial \mathcal{H}}{\partial \mathbf{p}} = \mathbf{A}\Delta\mathbf{T}^* + \mathbf{B}\mathbf{u}^*, \quad (25)$$

$$\dot{\mathbf{p}}^* = -\frac{\partial \mathcal{H}}{\partial \Delta\mathbf{T}} = -\mathbf{F}'\mathbf{F}'^T \Delta\mathbf{T}^* - \mathbf{A}\mathbf{p}^* + r\mathbf{F}', \quad (26)$$

with boundary conditions  $\Delta\mathbf{T}^*(t_0) = \Delta\mathbf{T}_0$  and  $\mathbf{p}^*(t_f) = 0$ , where  $\mathbf{u}^*$  satisfies  $\mathcal{H}(\Delta\mathbf{T}^*, \mathbf{u}^*, \mathbf{p}^*, t) \leq \mathcal{H}(\Delta\mathbf{T}^*, \mathbf{u}, \mathbf{p}^*, t)$  such that

$$\mathbf{u}^* = \begin{cases} \mathbf{u}_{\min}, & \text{for } -\mathbf{R}^{-1}\mathbf{B}\mathbf{p}^* \leq \mathbf{u}_{\min} \\ -\mathbf{R}^{-1}\mathbf{B}\mathbf{p}^*, & \text{for } \mathbf{u}_{\min} < -\mathbf{R}^{-1}\mathbf{B}\mathbf{p}^* < \mathbf{u}_{\max} \\ \mathbf{u}_{\max}, & \text{for } -\mathbf{R}^{-1}\mathbf{B}\mathbf{p}^* \geq \mathbf{u}_{\max}. \end{cases} \quad (27)$$

Equation 27 represents the vector of time-dependent control signals allocated to  $n$  TCPMs which minimizes cost  $J$ . Substituting Equation 27 into Equation 25 results in a system of nonlinear ordinary differential equations with split boundary values. Solving this system results in optimal costates  $\mathbf{p}^*$  and thus optimal control  $\mathbf{u}^*$ .

### C. Influence of Weighting Matrix

Tracking cost  $J_t$  quantifies tracking performance. However, applying Pontryagin's minimum principle to the Hamiltonian defined by Equations 24 results in control that minimizes total cost  $J$ . Total cost  $J$  is a function of control effort cost  $J_c = \frac{1}{2} \int_{t_0}^{t_f} \mathbf{u}^T \mathbf{R} \mathbf{u} dt$ , which conserves control effort. With TCPM efficiency already on the order of 1% [1], TCPMs are not suitable for efficiency-critical applications. Conserving control effort is not a priority. Therefore, a small  $\mathbf{R}$  is selected such that that minimizing  $J$  effectively minimizes  $J_t$  independent of  $J_c$ . For a sufficiently small  $\mathbf{R}$ , further reducing  $\mathbf{R}$ , and therefore further reducing  $J_c$ , has negligible impact on  $J_t$ .

Weighting matrix  $\mathbf{R}$  represents the fundamental trade-off between performance and control effort. As  $\mathbf{R}$  approaches  $\mathbf{0}$ , Equation 27 converges to bang-bang control. If the rate of change of the reference is greater than the maximum rate of change of the system, the system will saturate and effectively act as a bang-bang controller. However, a bang-bang controller does not describe how to share control effort between actuators when the rate of change of the reference is less than what the system is capable of. Therefore, it does not resolve the redundancy inherent to a multi-input single-output system.

Some weight on controller effort is required to prevent bang-bang control. The relative weight of control effort should be independent of TCPM geometry, such that weighted effort is consistent across geometric configurations of TCPMs. The following diagonal weighting matrix as a function of scalar  $R_0$  is chosen:

$$R_{ii} = \frac{R_0}{nu_{\max_i}^2}. \quad (28)$$

Equation 28 results in control effort cost

$$J_c = \frac{1}{2} \int_{t_0}^{t_f} \sum_{i=1}^n \frac{R_0 u_i^2}{nu_{\max_i}^2} dt. \quad (29)$$

Equation 29, and the fact input  $u_i$  is constrained such that  $u_i \in [T_{\min}/K_i, T_{\max}/K_i]$ , bounds  $J_c$  such that

$$\frac{J_c}{t_f - t_0} \in \left[ \frac{R_0 T_{\min}^2}{2T_{\max}^2}, \frac{R_0}{2} \right]. \quad (30)$$

As a result, the bounds of  $J_c$  are not a function of the number of TCPMs in parallel  $n$  or of electrothermal steady state gain  $K_i$ , which is a function of TCPM geometry. Scalar  $R_0$  now quantifies the trade-off between performance and weighted control effort independent of TCPM geometry.

## IV. OPTIMIZATION

### A. Design Variables

TCPM tracking cost is minimized with respect to geometric parameters to determine the optimal tracking performance for heterogeneous and homogeneous bundles of  $n$  TCPMs. The geometry of any TCPM is described by nondimensional twist insertion  $\Phi$ , fiber diameter  $d$ , spring index  $C$ , stretch ratio  $w$ , and fiber length  $l$  (see Subsection II-A). The dependence of design variables on tracking performance is investigated to reduce the dimensionality of the optimization.

Fiber length  $l$  does not affect the range of realizable thermal forces, nor does it affect TCPM dynamics (see Subsection II-F). Thus, it can be ignored from the optimization without affecting cost.

Non-dimensional twist insertion  $\Phi$  also does not affect actuator dynamics. Without this trade-off between maximum force and dynamics, the largest possible value of  $\Phi$  is selected to maximize  $\tau_b$  per Equations 15-17. Twist insertion is constrained by the onset of autocoiling, which is a function of precursor fiber tension during twist insertion<sup>6</sup>  $F_m$ , axial Young's modulus  $E_1$ , and transverse shear modulus  $G_2$  such that [4] [30]

$$\Phi = \frac{2\sqrt{2\pi E_1}}{\pi G_2 d} \sqrt{F_m}. \quad (31)$$

The maximum fiber stress before fiber rupture is assumed to be independent of diameter such that maximum manufacturing tension  $F_m$  scales with fiber cross section  $d^2$ . As a result, maximum  $\Phi$  per Equation 31 is also independent of fiber diameter. Pilot experiments revealed a 0.8 mm nylon 6,6 fiber (Eurofysica, Spoeltje ijzerdraad) ruptured before the onset of autocoiling when fiber tension was greater the 5 N. Thus, a maximum value of  $\Phi = 0.70$  was selected, corresponding to an outer fiber bias angle of 35°. Pilot experiments were conducted on a custom TCPM manufacturer. The design of the manufacturing setup is detailed in Appendix A.

The maximum realizable stretch ratio  $w$  is dependent on spring index  $C$ . Autocoiled TCPMs typically have spring indices of approximately 2 and are capable of strokes up to 20% ( $w = 1.2$ ), while mandrel coiled TCPMs with  $C = 6$

<sup>6</sup>Wu and Zheng empirically validated this relationship for a 0.6 mm diameter fiber for twist insertions up to 3.1 rad/mm [18].

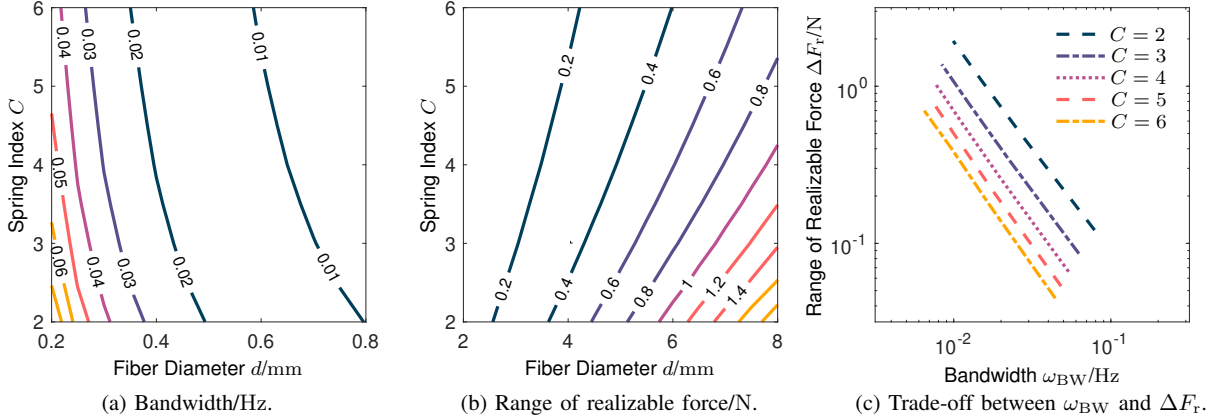


Fig. 8: Contour plots of (a) bandwidth  $\omega_{BW}$  and (b) range of realizable force  $\Delta F_r$  based on the linearized model of a single unidirectional TCPM. (c) TCPM geometry relates  $\Delta F_r$  to  $\omega_{BW}$  as shown for  $d \in [0.2\text{mm}, 0.8\text{mm}]$  and  $C \in \{2, 3, 4, 5, 6\}$ . The slope for  $C = 2$  is  $-1.3$ .

are capable of strokes up to 50% ( $w = 1.5$ ) [1]. Both the thermomechanical and electrothermal models are functions of stretch ratio  $w$ . Per Castigliano's method (Equation 19), the dependence of thermomechanical model on  $w$  is negligible for  $\pi^2 C^2 + 1 \gg w^2$ . This simplification is valid even for the worst case scenario of an auto-coiled TCPM with a stretch ratio of  $w = 1.2$  and  $C = 2$ . The variation in bandwidth  $\omega_{BW}$  due to  $w$  is small compared to that of the anticipated range of spring indices and fiber diameters. Because its effect on TCPM performance is minor, a constant stretch ratio of  $w_i = 1.2$  is selected, rather than included as a design variable.

Decreasing spring index  $C$  monotonically increases both bandwidth  $\omega_{BW}$  and range of realizable forces  $\Delta F_r$  due to the input constraints:

$$\Delta F_r = F'(T_{\max} - T_{\min}). \quad (32)$$

This monotonicity is not analytically apparent in Equations 5 or 19. However, it is visible over  $d \in [0.2\text{mm}, 0.8\text{mm}]$  and physically-realizable spring indices  $C \in [2, 6]$  as shown in Figure 8a and 8b. The trade-off between  $\Delta F_r$  and  $\omega_{BW}$  (see Figure 8c) represents the fundamental trade-off between low-force high-bandwidth TCPMs and high-force low-bandwidth TCPMs. Decreasing  $C$  is constrained by the onset of auto-coiling, such that  $C = 2$  is chosen to increase both  $\Delta F_r$  and  $\omega_{BW}$ .

Fiber diameter  $d_i$  for each TCPM  $i$  is thus the only nontrivial geometric parameter with respect to tracking performance. Figure 8 demonstrates increasing  $d_i$  increases range of realizable force while decreasing bandwidth. Tracking cost is therefore minimized with respect to fiber diameter  $d_i$  for  $n \in \{2, 3, 4\}$ , resulting in  $n$  design variables per optimization. Fiber diameters between 0.2 and 0.8 mm are considered, which are commercially available as finishing line or sewing thread. Hauser's convection coefficient model is valid for this range of fiber diameters in conjunction with the other specified geometric parameters.

## B. Numerical Methods

Each geometric optimization across  $n$  fiber diameters minimizes the tracking cost of the linearized system. Error in performance, and therefore tracking cost, is thus solely due to dynamic performance. It is not confounded with error associated with the linear approximation.

Matrices  $\mathbf{A}$ ,  $\mathbf{B}$ , and  $\mathbf{F}'$  describe the linear system per Equations 21 and 22. The electrothermal gain  $K_i$  and bandwidth  $\omega_{BW_i}$  are calculated per Subsection II-C to construct state matrix  $\mathbf{A}$  and input matrix  $\mathbf{B}$ . Numerically integrating Equation 17 provides blocked torque  $\tau_{b_i}$  as a nonlinear function of temperature  $T_i$  for each TCPM  $i$ . Applying a linear fit for  $T_i \in [T_{\min}, T_{\max}]$  results in a linear relationship between  $\tau_{b_i}$  and  $\Delta T_i$ . Output matrix  $\mathbf{F}'$  is then the element-wise product of the slope of this linear relationship and of temperature-independent thermal constant  $c_i$ .

Pontryagin's minimum principle determines optimal control and associated increase in actuator temperatures  $\Delta T$  per Section III. Optimal  $\Delta T^*$  is initially found for an arbitrary value of weighting matrix scalar  $R_0 = 0.2$ , which quantifies the trade-off between reducing tracking cost  $J_t$  and control effort cost  $J_c$ . The split-boundary-value problem described by Pontryagin's minimum principle (Equations 25 and 26) is solved using MATLAB's `bvp4c` function. This function implements the Lobatto IIIa collocation formula on integration subregions dictated by a specified initial mesh. If the residuals between the numerical and continuous solutions to the ordinary differential equations at any subregion exceed a specified tolerance, the mesh adapts and the numerical solution is reevaluated [31]. Memory limitations constrain maximum mesh density to an integer  $2 \times 10^6/n$  points.

Weighting matrix scalar  $R_0$  is iteratively halved and the split-boundary-value problem reevaluated until the tracking cost  $J_t$  of two subsequent iterations converges within 2%. Further reducing weighted control effort thus has negligible impact on reducing tracking cost. As  $R_0$  is reduced, control approaches bang-bang control. Mesh convergence within the

bvp4c function thus becomes highly sensitive to switching times and therefore mesh densities. To improve mesh convergence, the numerical solution and mesh produced by each iteration is provided as an initial guess to the subsequent iteration. If mesh density is exceeded, the initial step in  $R_0$  is decomposed into recursively smaller subintervals. Evaluating the split-boundary-value problem for each subinterval produces a guess solution and mesh for the next subinterval. This is repeated until a guess is produced that enables evaluating the split-boundary-value problem for the initial step in  $R_0$  without exceeding the mesh density limit. Appendix B contains pseudocode that implements tracking cost convergence with respect to  $R_0$  as described.

### C. Brute-Force Investigation

Multiple brute-force investigations computed optimal tracking cost for  $n \in \{2, 3, 4\}$  unidirectional TCPMs in parallel, and for  $n = 2$  pairs of antagonistic TCPMs in parallel. All investigations considered fiber diameters between 0.2 mm and 0.8 mm. For  $n = 2$  TCPMs in parallel, unidirectional-bundle fiber diameters were incremented by 0.5 mm, while antagonistic-bundle diameters were incremented by 1 mm. All other  $n$ -dimensional heterogeneous investigations incremented fiber diameter by 2 mm. All 1-dimensional homogeneous investigations incremented fiber diameter by 0.25 mm.

All previously described brute-force investigations were repeated for each reference signal shown in Figure 9. Each reference signal  $r_F$  has a range of  $r_F \in [F_{\min}, F_{\min} + 1\text{N}]$ . Because input saturation constrains minimum temperature  $T_{\min}$ ,  $F_{\min}$  is the minimum thermal force the combination of  $n$  TCPMs can produce:  $F_{\min} = \sum F'_i(T_{\min} - T_a) + \sum F_{a_i}$ . An initial condition of  $\Delta T_0 = T_{\min} - T_a$  was provided such that tracking error is not dominated by the transient response from an initial offset.

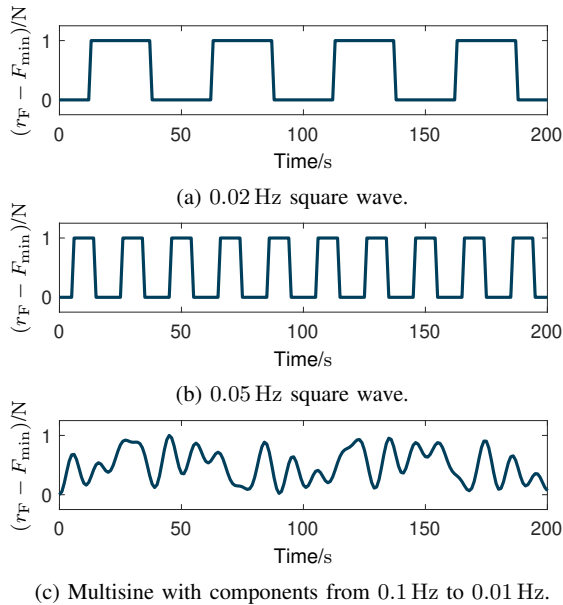


Fig. 9: Reference signals defined with respect to minimum realizable force  $F_{\min}$ .

Multisine tracking performance was investigated to assess if square-wave tracking results were generalizable to less specific tracking tasks. The multisine in Figure 9c was constructed in a similar manner as [16] to mitigate sharp peaks. It consists of 5 components:

$$r_F(t) = b + a \sum_{i=1}^5 \sin(2\pi f_i(t - t_0) + \theta_i), \quad (3F)$$

with component frequencies  $f_i$  evenly spaced between 0.01 and 0.1 Hz. Constants  $a$  and  $b$  scale and shift the reference such that  $r_F \in [F_{\min}, F_{\min} + 1\text{N}]$ . Time shift  $t_0$  ensures  $r_F(0) = F_{\min}$ , which corresponds to initial state condition  $\Delta T_0 = T_{\min} - T_a$ . Finally, phase offset  $\theta_i = \theta_0 - \pi i^2/5$ , where pseudo-randomly generated  $\theta_0 = 0.9058$  rad.

## V. RESULTS

All results shown are for TCPM geometries with spring indices of  $C = 2$ , outer fiber bias angles of  $35^\circ$  ( $\Phi = 0.70$ ), and stretch ratios of  $w = 1.2$  per Subsection IV-A. Results are from the linearized model unless explicitly stated.

Figure 10 shows unidirectional-configuration homogeneous-bundle tracking cost as a function of fiber diameter for all reference signals. It also shows tracking cost for heterogeneous bundles relative to the minimum homogeneous tracking cost for the corresponding reference signal. Figures 11, 12, and 13 show optimal control, temperature, and force predicted by the linear and nonlinear models as functions of time for each reference signal. Plots are displayed for the optimal  $n = 2$  homogeneous bundle of  $d = 0.45$  mm and an arbitrary heterogeneous bundle of  $d_1 = 0.4$  mm and  $d_2 = 0.8$  mm.

Figure 14 similarly shows relative tracking cost as a function of fiber diameters for heterogeneous bundles of  $n = 2$  antagonistic pairs of TCPMs. Relative tracking cost is defined with respect to minimum tracking cost, which was achieved by fiber diameters of  $d_1 = d_2 = 0.8$  mm. Time plots are contained in Appendix C.

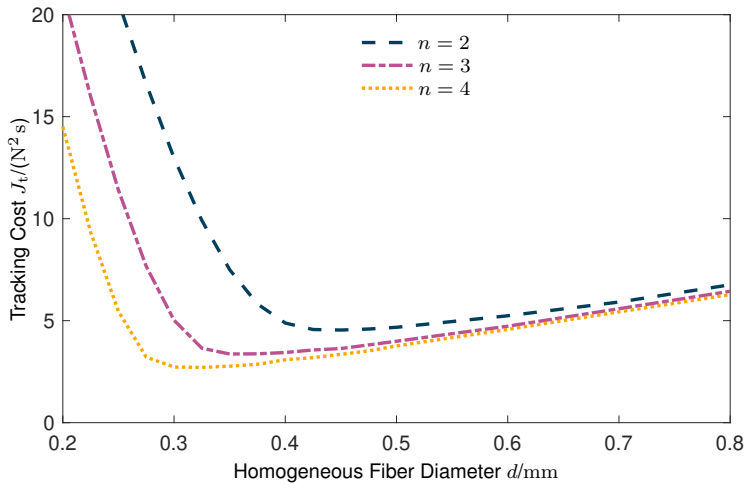
Figure 15 displays the optimal tracking of various sinusoidal force references by individual TCPMs ( $n = 1$ ) of varying diameters. Both unidirectional and antagonistic configurations are displayed for comparison.

Table II contains the minimum tracking costs, and corresponding optimal fiber diameter, predicted by the linear model for various homogeneous bundles and reference signals. The table also contains tracking cost of the nonlinear model fed the optimal control derived from the linear model.

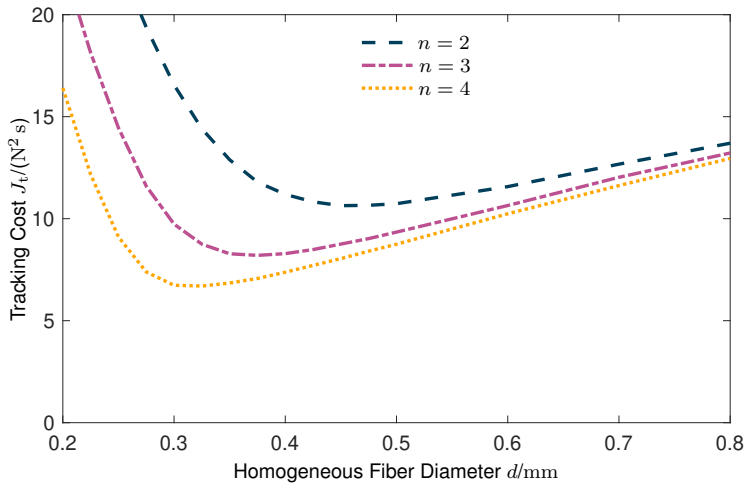
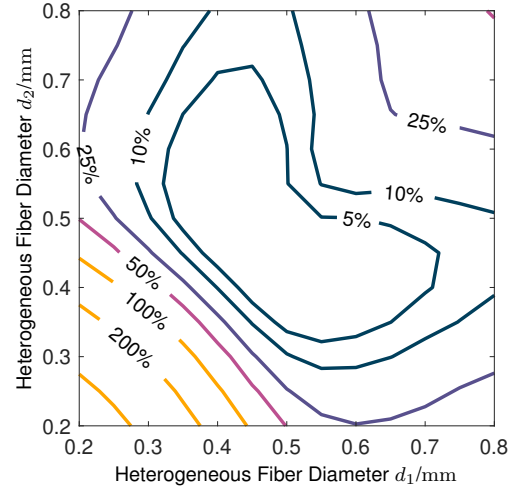
## VI. DISCUSSION

### A. Tracking Performance Improvement

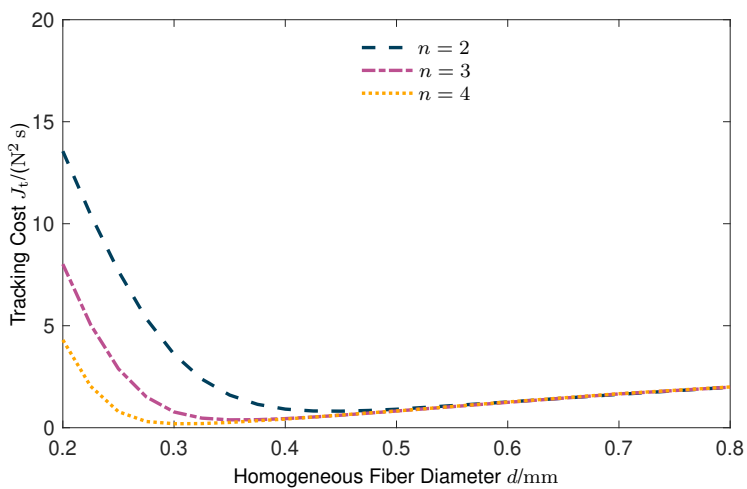
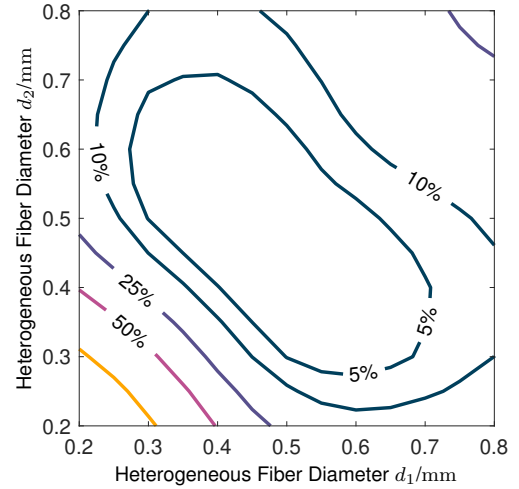
This work hypothesized that the force-tracking performance of heterogeneous bundles of  $n$  TCPMs in parallel would be substantially improved compared to that of homogeneous bundles. Force-tracking performance is defined as minimizing tracking cost  $J_t$ . The minimum homogeneous-bundle tracking cost outperformed all heterogeneous-bundle tracking costs identified via brute force (see Figures 10 and 14 respectively for unidirectional and antagonistic configurations of  $n = 2$ ).



(a) 0.02 Hz 0-1 N square-wave reference signal.



(b) 0.05 Hz 0-1 N square-wave reference signal.



(c) Multisine reference signal.

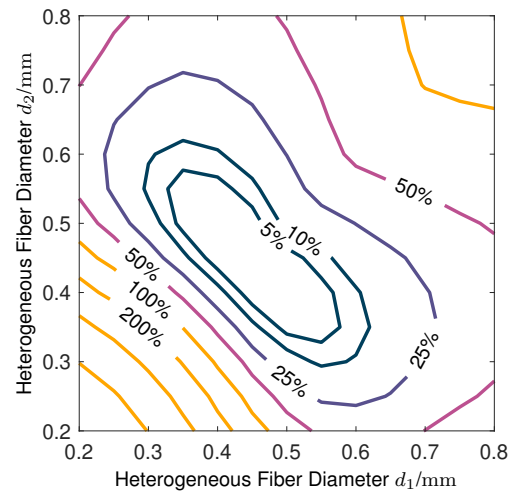


Fig. 10: Tracking cost  $J_t$  for unidirectional configurations of TCPMs for reference signals (a), (b), and (c). Left:  $J_t$  for homogeneous bundles of  $n$  TCPMs in parallel as a function of fiber diameter  $d$ . Right: Relative tracking cost for heterogeneous bundles of  $n = 2$  TCPMs in parallel as a function of fiber diameters  $d_1$  and  $d_2$ . Relative tracking cost is defined with respect to the minimum homogeneous-bundle tracking cost for  $n = 2$ .

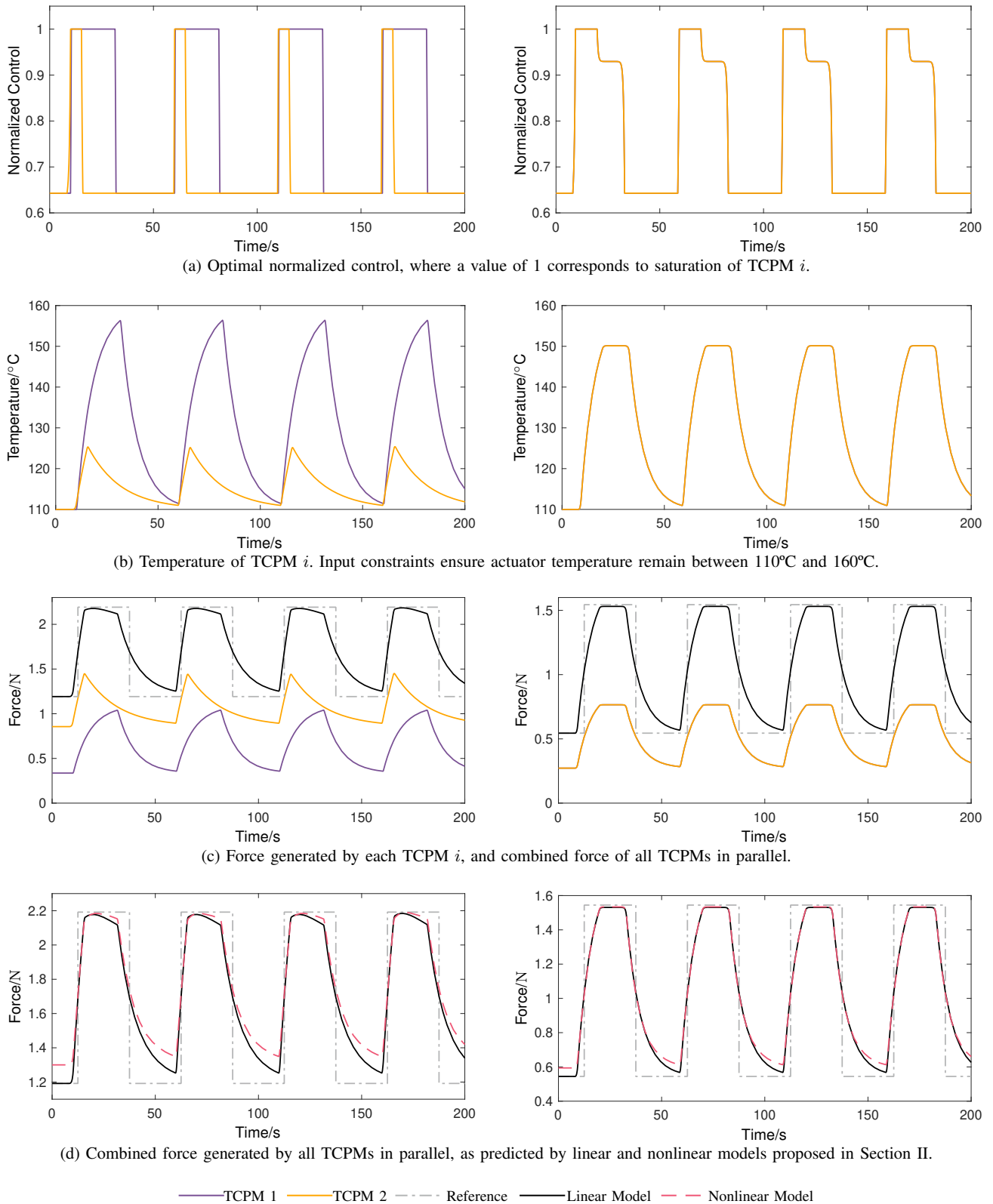


Fig. 11: (a) Optimal control, (b) temperature, and (c)(d) force as a function of time for  $n = 2$  unidirectional TCPMs in parallel. Left: response of the heterogeneous bundle with fiber diameters  $d_1 = 0.4$  mm and  $d_2 = 0.8$  mm. Right: response of the homogeneous bundle with optimal fiber diameter  $d = 0.45$  mm which minimizes tracking performance.

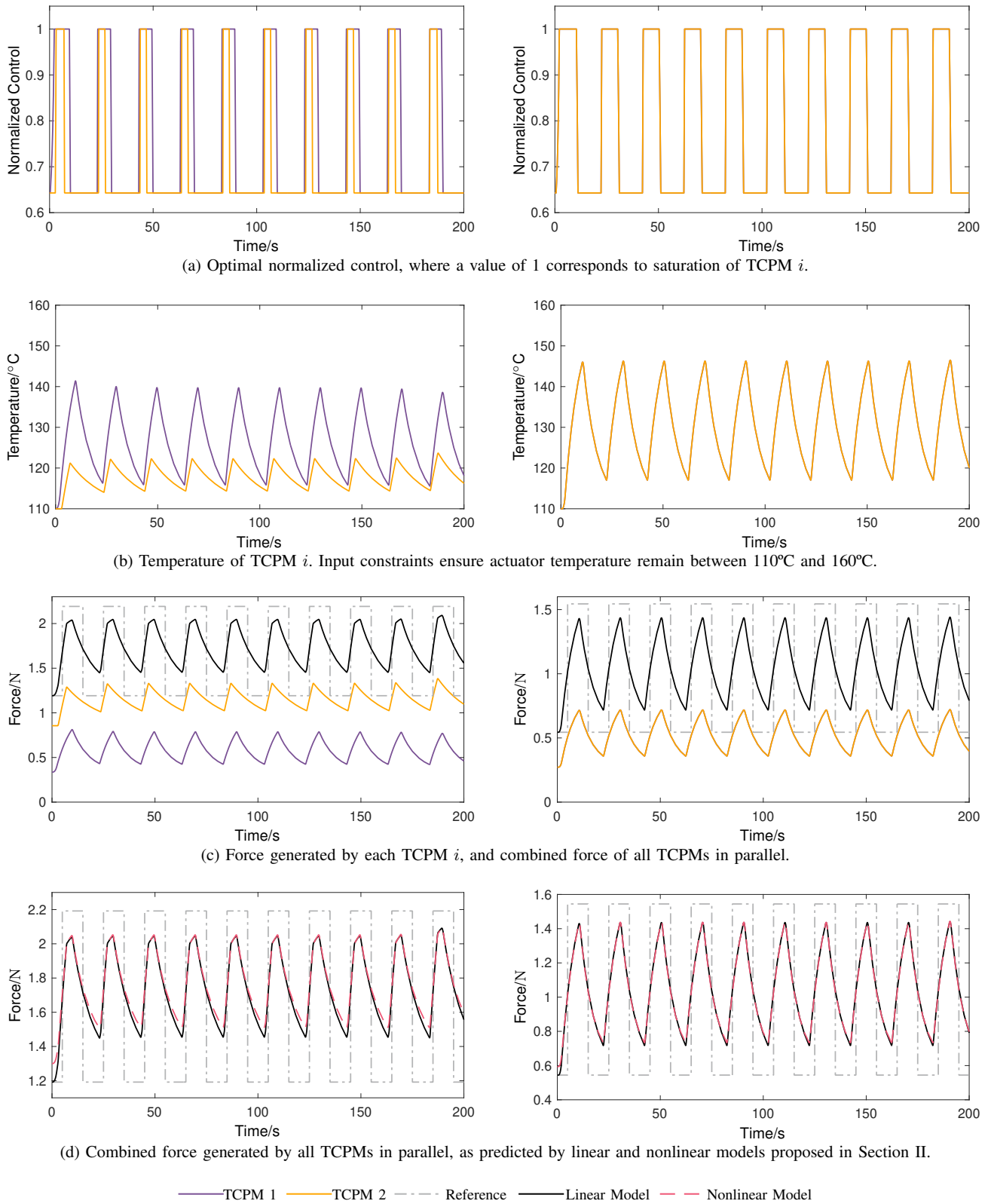


Fig. 12: (a) Optimal control, (b) temperature, and (c)(d) force as a function of time for  $n = 2$  unidirectional TCPMs in parallel. Left: response of the heterogeneous bundle with fiber diameters  $d_1 = 0.4$  mm and  $d_2 = 0.8$  mm. Right: response of the homogeneous bundle with optimal fiber diameter  $d = 0.45$  mm which minimizes tracking performance.

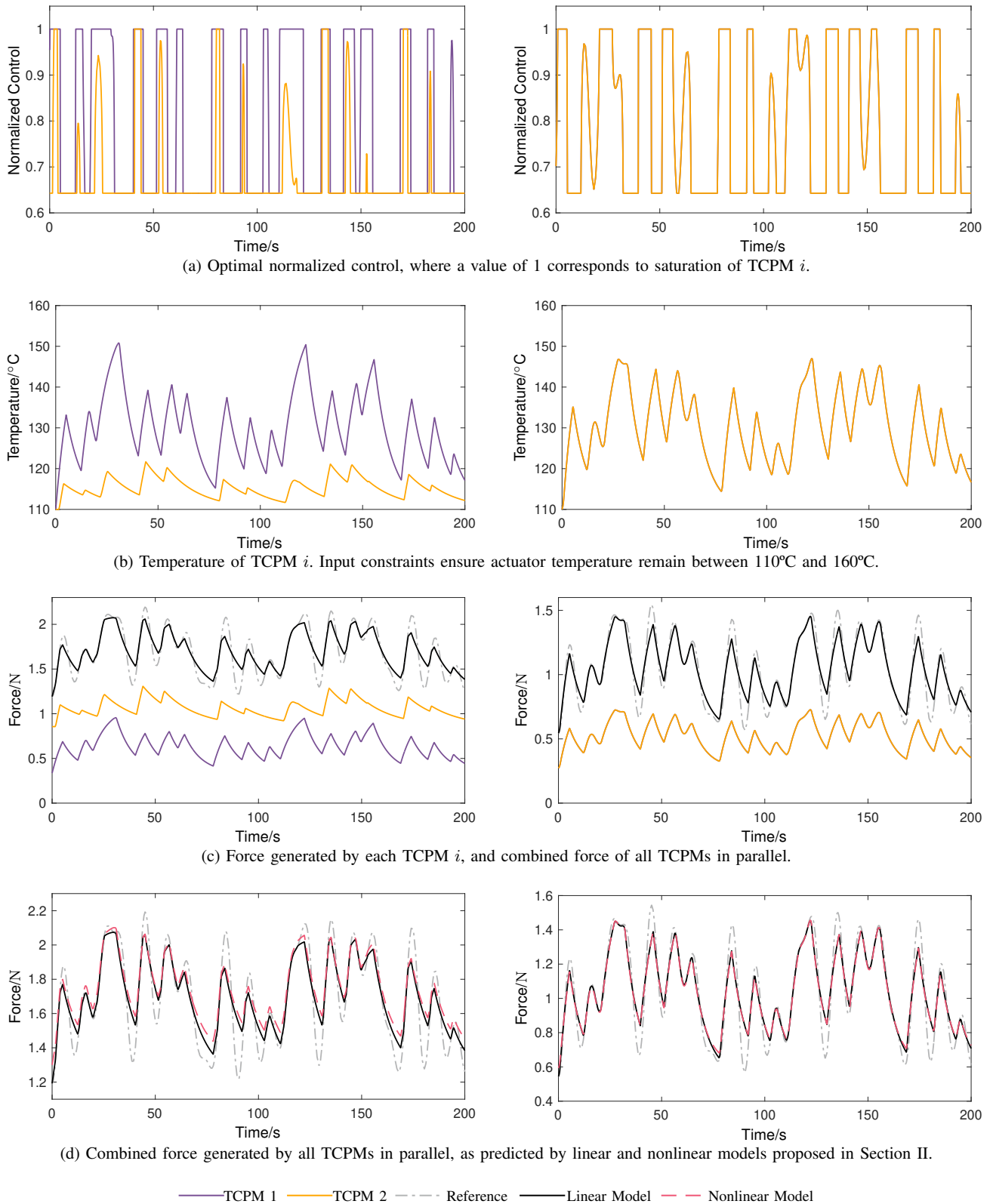


Fig. 13: (a) Optimal control, (b) temperature, and (c)(d) force as a function of time for  $n = 2$  unidirectional TCPMs in parallel. Left: response of the heterogeneous bundle with fiber diameters  $d_1 = 0.4$  mm and  $d_2 = 0.8$  mm. Right: response of the homogeneous bundle with optimal fiber diameter  $d = 0.45$  mm which minimizes tracking performance.

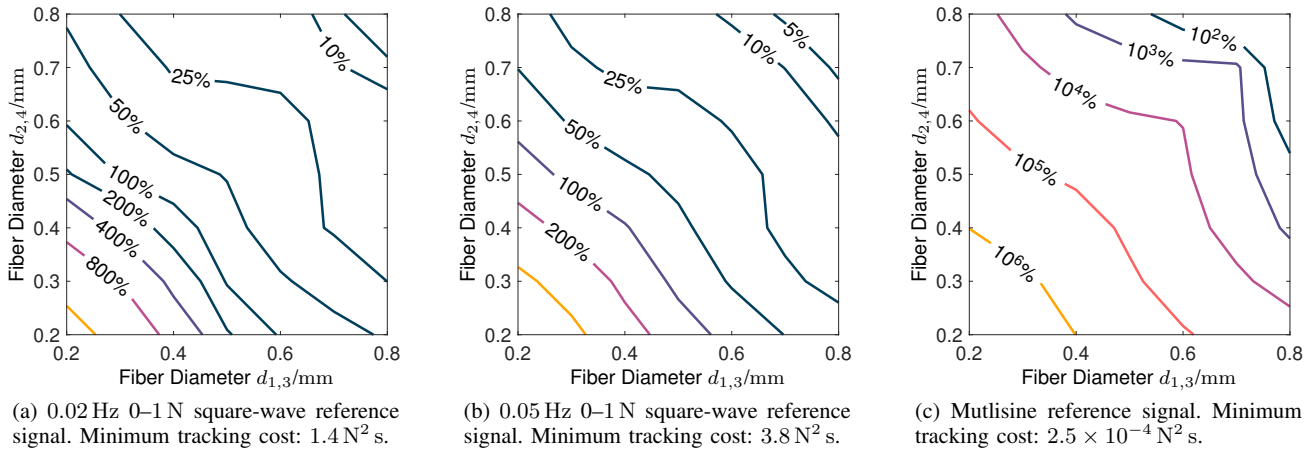


Fig. 14: Relative Tracking cost  $J_t$  for antagonistic configurations of heterogeneous bundles ( $n = 2$ ) for reference signals (a), (b), and (c). Relative tracking cost is defined with respect to the minimum homogeneous-bundle tracking cost, which occurs at fiber diameters  $d_1 = d_2 = 0.8 \text{ mm}$ . Note that  $J_t$  is monotonic with  $d$  for antagonistic configurations.

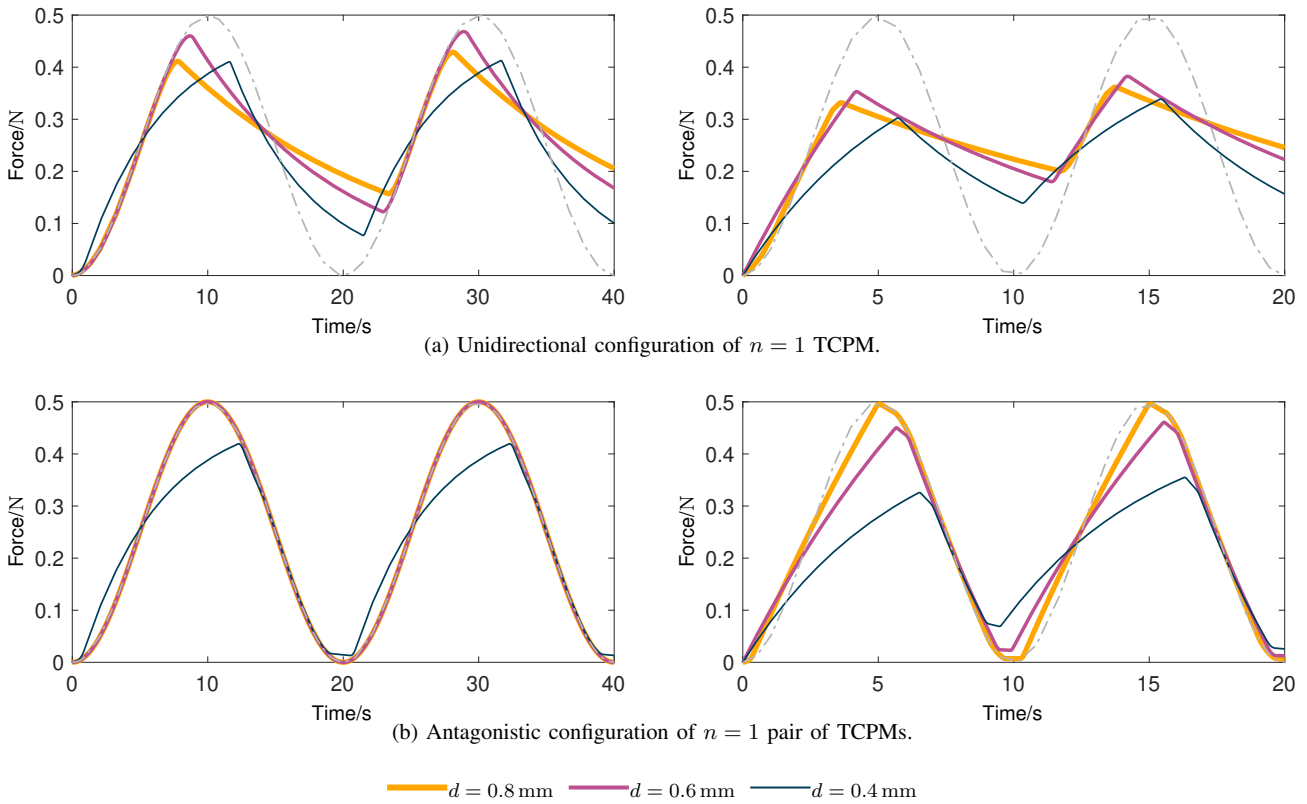


Fig. 15: Optimal force tracking of 0.05 Hz and 0.1 Hz sinusoidal references by individual TCPMs ( $n = 1$ ) of varying diameters. Fiber diameters of  $d = 8, 6,$  and  $4 \text{ mm}$  correspond to TCPM bandwidths of  $\omega_{\text{BW}} = 0.01, 0.03,$  and  $0.08 \text{ Hz}$ , respectively.

TABLE II: Tracking error of various homogeneous bundles with respect to reference signals  $r_F$  shown in Figure 9. Bundles consist of  $n$  unidirectional TCPMs in parallel, or of  $n$  antagonistic pairs of TCPMs, with fiber diameter  $d$  that minimizes tracking cost  $J_t$  of the linear model. Nonlinear tracking cost is calculated by feeding the nonlinear model the optimal control derived from the linear model.

$r_F$	$n$	$d/\text{mm}$	Unidirectional		Antagonistic	
			Linear $J_t/(\text{N}^2 \text{ s})$	Nonlinear $J_t/(\text{N}^2 \text{ s})$	Linear $J_t/(\text{N}^2 \text{ s})$	Nonlinear $J_t/(\text{N}^2 \text{ s})$
(a)	2	0.45	4.5	4.8	1.4	2.7
(a)	3	0.35	3.4	3.5	—	—
(a)	4	0.32	2.7	2.9	—	—
(b)	2	0.45	10.6	10.8	3.8	4.8
(b)	3	0.38	8.3	8.4	—	—
(b)	4	0.32	6.7	6.9	—	—
(c)	2	0.45	0.81	0.85	0.00025	0.52
(c)	3	0.35	0.39	0.40	—	—
(c)	4	0.30	0.20	0.23	—	—

This was the case for all reference signals, number of TCPMs in parallel ( $n \in \{2, 3, 4\}$  for unidirectional actuation), and for both unidirectional and antagonistic configurations ( $n = 2$ ). Homogeneous bundles of the optimum fiber diameter thus outperform heterogeneous bundles, invalidating the proposed hypothesis.

### B. Unidirectional Actuation

Tracking cost  $J_t$  is convex with respect to fiber diameter  $d$  for unidirectional actuation of heterogeneous bundles, as shown in Figure 10. Note that  $d$  is the only geometric parameter that is nontrivial with respect to force-tracking performance, as demonstrated in Subsection IV-A. This apparent convexity suggests heterogeneous bundle performance only improves as it converges on the optimal homogeneous bundle. No local or global minima appear in regions with a substantial difference in fiber diameter. Even the best performing heterogeneous bundles of substantially different fiber diameters have an average fiber diameter close to that of the optimal homogeneous bundle, suggested by the oblong shape of the 5% contours in Figure 10.

Choice of reference signal has little effect on tracking cost as a function of fiber diameter. The optimal unidirectional homogeneous fiber diameter, assumed to be the global minimizer, is  $d = 0.45$  mm for all reference signals. Contour shapes are generally similar between reference signals. Figure 10c reveals multisine relative tracking performance is slightly more sensitive to deviations from optimal homogeneous fiber diameter. This is because the minimum tracking cost is substantially less than that of the square-wave references, as each square-wave corner causes a large spike in tracking error.

The maximum rates of heating and cooling for unidirectional TCPMs are a function of actuator temperature  $T$ , and are not necessarily the same value. Rearranging Equation 1 in terms of electrothermal model parameters  $\omega_{\text{BW}}$  and  $K$ , the rate of temperature change is

$$\dot{T} = \omega_{\text{BW}}(Ku - T + T_a), \quad (34)$$

where  $Ku \in [T_{\min}, T_{\max}]$  to ensure operation in the linear region. Because  $T \in [T_{\min}, T_{\max}]$ , the maximum possible rate of heating for unidirectional TCPMs is greater than that of cooling:

$$\frac{\dot{T}}{\omega_{\text{BW}}} \in [T_a + (T_{\max} - T_{\min}), T_a - (T_{\max} - T_{\min})]. \quad (35)$$

This heating-cooling asymmetry is particularly apparent in Figures 11 and 12, where the error is dominated by cooling dynamics.

Optimal control allocates the reference signal between unidirectional heterogeneous actuators as shown in Figures 11, 12, and 13. During rapid increases in reference force, such as during the leading edges of square waves, control of both actuators saturate. Immediately before instances of rapid cooling and if all actuators are not already saturated, more normalized control effort is allocated to the high-bandwidth smaller-diameter actuator. High-bandwidth actuator temperature is therefore maximized to minimize Equation 34 on the onset of cooling. The high-bandwidth fiber reaches maximum temperature immediately before rapid drops in reference force, exemplified by the trailing edge of square waves in Figures 11 and 12, and at times 32 s and 123 s in Figure 13. Based on only this qualitative description of optimal control allocation, it is unclear if or to what extent allocating control between heterogeneous TCPMs improves tracking performance compared to homogeneous TCPMs. Numerical evaluation across a range of fiber geometries ultimately reveals optimal homogeneous unidirectional bundles outperform all heterogeneous unidirectional bundles.

### C. Antagonism

Determining the optimal antagonistic configuration is trivial, suggested by the monotonic trend of increasing fiber diameter and decreasing tracking cost shown in Figure 14. Heating dynamics drive both increasing and decreasing force in antagonistic configurations. Optimal antagonistic TCPM geometries thus try to decrease actuator temperature to increase the maximum possible rate of heating, rather than minimize or maximize temperature before respective periods of rapid heating or cooling.

The triviality of fiber diameter selection for antagonistic configurations is highlighted by Figure 15b. Antagonistic TCPMs outperform TCPMs of smaller fiber diameters for all shown sinusoidal tracking tasks. This is not the case for unidirectional TCPMs shown in Figure 15a. Predictive control ensures no phase lag between reference and TCPM response, even when reference frequency is substantially higher than TCPM bandwidth. The low bandwidth of TCPMs with large diameter fibers imply a long settling time. However, the corresponding increase in range of realizable forces  $\Delta F_r$  ensures the maximum rate of change of thermal force  $\dot{F}$  is larger than that of any TCPM with a smaller diameter fiber (see first 5 seconds of Figure 15b(right)).

The fundamental trade-off between  $\Delta F_r$  and  $\omega_{\text{BW}}$  determines if the maximum  $\dot{F}$  is greater than that of any higher-bandwidth TCPM. Equation 22 implies  $\dot{F} = F'\dot{T}$  such that

$\dot{F} \propto F' \omega_{\text{BW}}$  per Equation 34. Figure 8c shows  $F' \propto \omega_{\text{BW}}^{-1.3}$ . In total  $\dot{F} \propto \omega_{\text{BW}}^{-0.3}$ , meaning low-bandwidth TCPMs produce both a greater maximum rate of change of force and larger range of realizable forces. This rationale is only valid for antagonistic configurations. Per Equation 34 these configurations only consider heating dynamics. Optimal geometries always maximize  $\dot{T}$  and  $\dot{F}$  by minimizing actuator temperature  $T$ . If  $\dot{F}$  was proportional to  $\omega_{\text{BW}}$  raised to a power greater than  $-1$  (slope of Figure 8c greater than  $-1$ ), it is hypothesized that antagonistic actuator selection would no longer be trivial. This may be the case for antagonistic artificial muscles other than TCPMs that also have first-order dynamics.

#### D. Spring Index

Decreasing spring index increases TCPM bandwidth  $\omega_{\text{BW}}$  and the thermal force generated per blocked torque  $c$ . A larger  $\omega_{\text{BW}}$  and  $c$  suggest spring index should be minimized to maximize isometric force-tracking performance. Spring index is ultimately constrained by the onset of spontaneous coiling nucleation during twist insertion. Therefore, auto-coiled TCPMs outperform homochiral mandrel-coiled TCPMs in isometric force tracking. Note that auto-coiled TCPMs are exclusively homochiral. Mandrel coiling is still required to manufacture heterochiral TCPMs of a small spring index.

Increasing spring index provides benefits outside the context of isometric feedforward force tracking. Spring index influences coil inductance, where a small index may negatively affect self-sensing ability when applicable. Thus, for closed-loop control applications, a small spring index may have an indirect negative effect on tracking performance by degrading the quality of the self-sensed measurement signal. Spring index also influences range of length contraction. TCPMs with a spring index of  $C = 6$  are able to achieve 50% contraction, compared to a maximum 20% contraction for auto-coiled TCPMs ( $C \approx 2$ ) [4].

For isotonic position tracking, length contraction  $\Delta L$  is linear with  $f_2 \tau_b$  per Castigliano's method (Equation 18). In this case, decreasing fiber diameter increases both bandwidth and thermomechanical gain such that spring index selection becomes nontrivial. A heterogeneous configuration would thus consist of a single TCPM with the smallest fiber diameter required to prevent failure under load. The TCPM spring index would be nonuniform, with an optimal controller regulating the temperature of different regions of the TCPM. However,  $f_2 \propto \omega_{\text{BW}}^{-7}$  such that the maximum rate of length contraction  $\dot{L} \propto \omega_{\text{BW}}^{-6}$  for an antagonistic configuration. Thus, maximizing spring index minimizes antagonistic position-tracking cost.

#### E. Nonlinearity

Tracking error predicted by the linear and nonlinear models of optimal unidirectional homogeneous bundles differs by less than 8%<sup>7</sup> per Table II. Error caused by the slower cooling dynamics thus dominates tracking cost for unidirectional configurations. This renders the error associated with the linearization of blocked torque negligible, which is not the case for

<sup>7</sup>The linear and nonlinear models differ by 15% for  $n = 4$  unidirectional multisine tracking.

the optimal antagonistic homogeneous bundle. The improved dynamic performance of antagonistic configurations reduces overall tracking error, which makes the relative contribution of the linearization error more pronounced. Minimum antagonistic tracking error between linear and nonlinear models differs by multiple orders of magnitude per Table II.

The temperature nonlinearity is characterized by an increase in slope at around 80°C followed by an extended approximately linear region, as shown in Figure 7. Experiments conducted by Haines et al. [1] and Tang et al. [10] show the same qualitative nonlinear behavior in nylon 6,6 TCPM tensile actuation. Tang et al. hypothesize the nonlinearity is caused by the increase in axial thermal expansion coefficient above 80°C [10]. However, Tang et al. and this work ignore the substantial temperature dependence of elastic moduli, which may decrease by a factor of 4 between 110°C and 160°C [32]. It is also unclear if Tang et al. accounted for the temperature dependence of elastic moduli per [33] when measuring axial thermal expansion coefficient as a function of temperature, which is also used in this work.

The temperature dependence of both elastic material properties and thermal expansion coefficients substantially impact TCPM nonlinearity. However, these properties as a function of temperature also vary substantially within literature due to variation between nylon 6,6 fibers and testing conditions. Tang et al. are the only authors that experimentally determines both axial and transverse nylon 6,6 elastic moduli and nylon 6,6 axial thermal expansion coefficient for same testing conditions [10], although they only consider axial thermal expansion coefficient temperature-dependent. Notably, Choy et al. separately investigate nylon 6,6 thermal expansion coefficients [34] and stiffness matrix coefficients [32] for the required temperature ranges of this work. However, draw ratio, moisture sensitivity, and other manufacturing and environmental parameters significantly affect material properties between fibers and testing conditions. As a result, selectively implementing different material properties across literature, such as from [34] and [32], results in nonlinear behavior that does not agree with the qualitative trends discussed above.

Above the glass transition temperature, polymers possess greater intermolecular mobility which can result in substantial changes in material properties [35]. The glass transition temperature of nylon 6,6 is highly moisture dependent, varying from 100°C for desiccated nylon 6,6 to 0°C for 8%-water-content-by-mass nylon 6,6 [32]. Thus, moisture content may substantially affect minimum operating temperature  $T_{\text{min}}$ . Large moisture contents may even result in a linear thermo-mechanical model such that  $T_{\text{min}} = T_a$  and minimum input  $u_{\text{min}} = 0 \text{ V}^2$ .

## VII. CONCLUSION

This work investigated if the simulated force-tracking performance of TCPM bundles of heterogeneous geometries was substantially superior to that of homogeneous geometries. Tracking performance is a function of spring index and fiber diameter, among other geometric parameters. TCPM geometry governs the trade-off between actuator bandwidth

and maximum realizable actuator force. Decreasing spring index increases both bandwidth and maximum force such that auto-coiled TCPMs are always preferred for isometric force-tracking tasks. For unidirectional configurations of TCPMs, the relationship between tracking performance and fiber diameter is nontrivial. For antagonistic configurations, increasing fiber diameter monotonically improves tracking performance. The optimal homogeneous bundles outperformed all considered heterogeneous bundles for both unidirectional and antagonistic configurations across 3 reference signals.

Heterogeneous actuator bundles may be advantageous outside the scope of this work. This work assigned control to redundant TCPMs via an optimal predictive feedforward controller. Disturbance and noise rejection via closed-loop control was not considered. The self-sensing ability of TCPMs allow for low-cost implementation of closed-loop control. This context may further accentuate the advantages of heterogeneous actuators, where high-force actuators track a low-frequency reference and low-force actuators contribute to high-frequency disturbance and noise rejection. Additionally, heterogeneous bundles may outperform homogeneous bundles of artificial muscles with a different geometric trade-off between bandwidth and maximum realizable force.

## APPENDIX A PROPOSED TCPM MANUFACTURING SETUP

### *Introduction*

A custom TCPM manufacturer was developed to address limitations of previous methods of manufacturing TCPMs. The proposed setup is available at TU Delft. This setup was designed to repeatedly manufacture mandrel-coiled TCPMs, as automated methods for manufacturing auto-coiled TCPMs are well-established in literature.

Only one work in literature proposes an automated method of coiling mandrel-coiled TCPMs [36]. Three motors are used: one to twist the fiber, one rotate the mandrel, and one to translate the mandrel to set coil pitch. While this method is viable, recreating such a setup was beyond the scope of this work. Two different methods of manufacturing TCPMs were previously proposed at TU Delft. Both methods had limitations, as detailed in the subsection's below. To address these limitations, a new method for mandrel-coiled TCPM manufacturing is proposed.

This work ultimately concluded auto-coiled TCPMs outperform mandrel-coiled TCPMs for isometric force-tracking tasks. Therefore, further work on this setup was abandoned.

### *Previous Method of Manual TCPM Manufacturing*

TCPMs manufactured at TU Delft were previously constructed as described by [13]. While TCPMs constructed for [13] and [16] were repeatable, TCPMs constructed for other master's theses were not. This variability suggests the manufacturing method is highly skill-dependent.

This procedure has the following features and limitations:

- Feature: Twist insertion and mandrel coiling are conducted under constant and uninterrupted fiber tension.

- Limitation: Twisting speed is variable, which may affect TCPM repeatability [37].
- Limitation: Number of twists inserted per length is not controlled, as neither fiber length nor motor speed is controlled.
- Limitation: Manufacturing is time consuming because 4 fixation steps (crimping, knot tying, etc.) are required. First, both ends of the fiber must be fixed before twisting. After twisting and before coiling, one of end of the mandrel must be fixed to the twisted fiber. After coiling, the other end of the fiber must be fixed to the mandrel.

### *Previous Method of Automated TCPM Manufacturing*

Figure 16 shows an alternate previously-proposed and constructed TCPM manufacturer. This setup is capable of continuously producing twisted fiber. The motor on the right rotates the large central spindle at a constant speed. One spool of precursor fiber and one spool of heating-element wire are located within the spindle. Both fibers are fed through a first set of pulleys anchored to the spindle. A set screw determines the maximum clearance between the pulleys, and thus friction as the fiber is pulled between the pulleys. Fiber tension is therefore determined by the torque applied to a set screw. The fiber and wire are then fed through a second set of pulleys anchored to the frame on the left. A smaller speed-controlled motor and encoder attached to the second set of pulleys draws the fiber and wire at a constant feed rate.

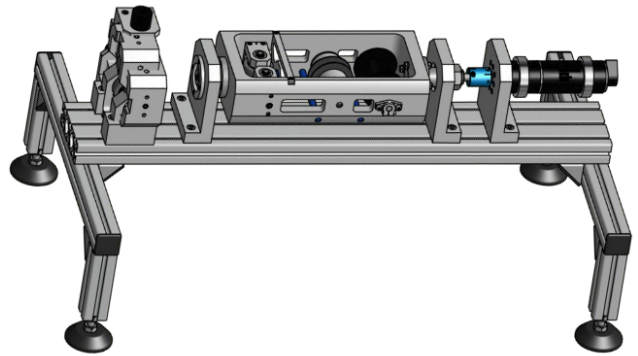


Fig. 16: Machine capable of continuously producing twisted fiber. As shown, the machine consists of 2 brushed DC motors, 2 sets of 2 pulleys, and a large spindle.

As displayed, this configuration is only capable of producing twisted-but-not-coiled fibers. Using an additional motor and linear motor to control mandrel coiling was proposed, but never implemented.

This procedure has the following features and limitations:

- Feature: Number of twists inserted per length is controlled by syncing the speeds of the large and small motors.
- Feature: Rate of twist insertion is tightly controlled.
- Feature: In theory, only two fixation steps are required: one to fix the continuously drawn twisted fiber to each side of the mandrel.

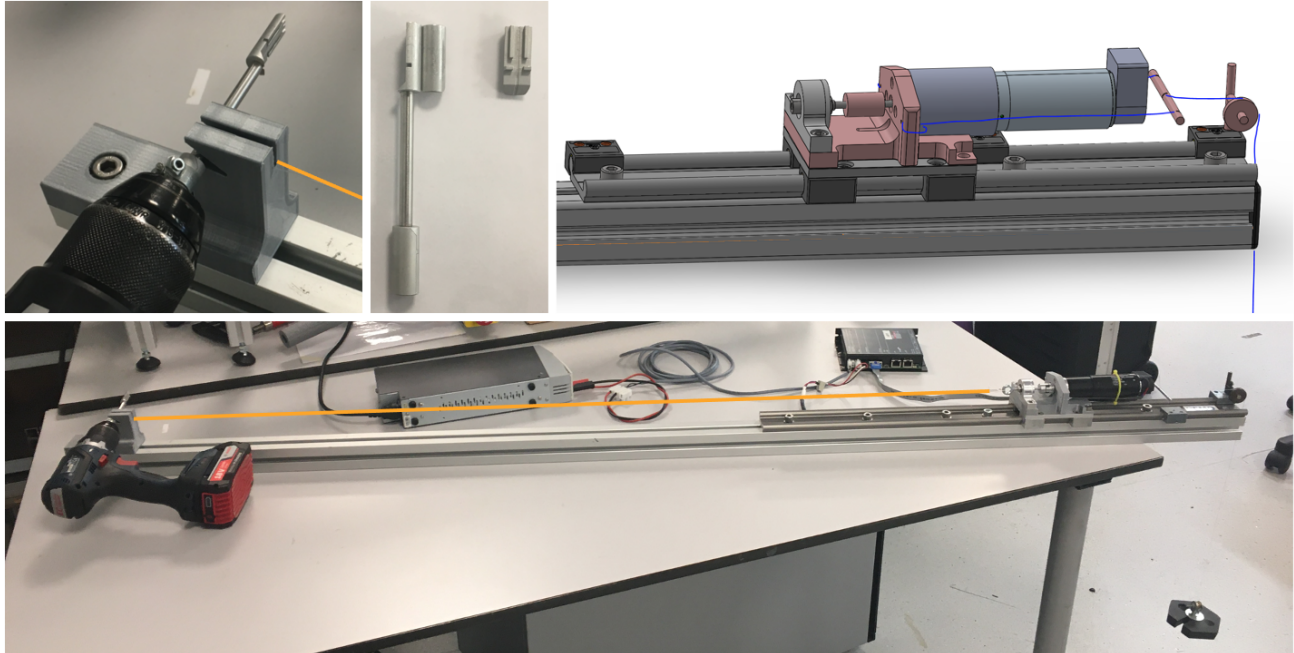


Fig. 17: Machine proposed to address current limitations of manufacturing mandrel-coiled TCPMs. The setup consists of a hand drill, a plastic mount, the mandrel, a paperclip, a brushed DC motor with encoder, driving electronics, a sled, and a weight. The precursor fiber is highlighted for clarity. The 4-piece mandrel previously developed at TU Delft is also shown.

- Limitation: Friction between pulleys determined by torque applied to a set screw is an indirect way to control fiber tension. Fiber tension must be very consistent to ensure a repeatable onset of autocoining.
- Limitation: The pulleys are observed to wear with time, further reducing fiber-tension consistency.

#### Proposed Design Requirements

Based on the observed features and limitations of previous TCPM manufacturing methods, the design requirements for a new manufacturer are:

- 1) *Constant tension.* The fiber must be held at a constant and uninterrupted tension throughout both the twisting and coiling process. This ensures a consistent onset of autocoining.
- 2) *Constant twist insertion per length.* The fiber length and number of twists inserted both must be repeatable. Therefore, twists inserted per length is also repeatable.
- 3) *Reduced number of fixations.* The number of fixation steps allowed is limited to 2. This reduces manufacturing time.

#### Proposed Method of Automated TCPM Manufacturing

Figure 17 shows the proposed TCPM manufacturer. It consists of a position-controlled Maxon 377622 brushed DC motor with encoder. The EPOS3 positioning controller (Maxon) is powered by a LSP-1403 DC power supply (Votcraft). The motor is mounted on a sled that can translate with one degree of freedom. The sled is contained on the track via a hard

stop on either end. A string connected to a weight is fed over a pulley and attached to the sled. It is attached such that the string tension the sled experiences acts through the motor axis. A hook protrudes from the sled which is attached to the motor via a shaft collar. The hook is supported by a bearing such that axial load from the hook acts through the bearing and not the motor. A stationary plastic mount is attached to the other end of the T-slotted aluminum.

The proposed manufacturing procedure is as follows:

- 1) Attach the precursor fiber and heating-element wire to the mandrel.
- 2) Place the mandrel in the chuck of a hand drill. Align the mandrel in the plastic mount as shown.
- 3) Tie a single loose slip knot using both the fiber and wire through a paperclip. The slip knot should be located about 1 m away from the mandrel-fixation point.
- 4) Place a spacer (not shown) in between the hard stop located closer to the center of the T-slotted aluminum and the sled.
- 5) Hook the paper clip into the hook protruding from the motor axle. Pull the slip knot tight such that the sled contacts the spacer and the spacer contacts the hard stop. The weight ensures the fiber is under tension while the knot is tightened. The spacer ensures the distance between the mandrel and the knot is repeatable.
- 6) Remove the spacer. Use the EPOS3 driver to rotate the motor a fixed number of revolutions.
- 7) Remove the mandrel from the plastic mount. Use the hand drill to rotate the mandrel and coil the fiber. Ensure the sled does not contact the hard stops on either end of

the track while coiling.

- 8) Wrap the paper clip around the mandrel to effectively crimp it in place. Alternatively, it may be more repeatable to use the 4-piece mandrel (shown in Figure 17) to constrain the coiled fiber. Further investigation is required, as this adds an extra fixation step.

This procedure meets the specified design requirements, as detailed below.

- 1) *Constant tension.* The weight-sled system ensures the fiber is under constant tension during twisting and coiling. Note the pulley generates substantially more friction than expected. To alleviate this issue, the pulley should be removed and the setup oriented vertically.
- 2) *Constant twist insertion per length.* The position-controlled motor tightly controls twist insertion. Manufacturing procedure steps 2-5 control fiber length.
- 3) *Reduced number of fixations.* Initially fixing the precursor fiber to the mandrel reduces one fixation step compared to the previous method of manual TCPM manufacturing. Crimping the paperclip to the mandrel is so easy it effectively does not count as another fixation step. The total number of fixation steps is then two.

## APPENDIX B

### PSEUDOCODE FOR TRACKING COST CONVERGENCE

The following pseudocode iteratively halves weighting matrix scalar  $R_0$  until tracking cost  $J_t$  converges between 2 successive iterations within 2% (see Subsection IV-B). Scalar  $R_0$  dictates the relative contributions of tracking cost and control effort cost to total cost, which optimal control minimizes. Using a provided guess mesh and solution, pseudocode function `solveSBVP(R0, guess)` solves the split-boundary-value problem defined by Equations 25 and 26 which are a function of  $R_0$ . The pseudocode is robust to mesh density limit errors. If mesh density limit is exceeded, the initial step in  $R_0$  is broken into recursively smaller subintervals. The `saveCosts.m` function that implements this pseudocode is available on GitHub (<https://github.com/imcginty/TCPM-Optimal-Force-Tracking>), along with all other code used to model TCPMs and allocate control.

```
[Jt, guess] = halveR0(R0, 0, 1, initialGuess)
loop until Jt converges
    R0 = R0/2
    [Jt, guess] = halveR0(R0, 0, 1, guess)

function [Jt, guess, x] = halveR0(R0, x, dx, guess)
loop until x = 1
    [Jt, newGuess] = solveSBVP(R0/(1+x+dx), guess)
    if maximum mesh density is exceeded
        [Jt, guess, x] = halveR0(R0, x, dx/2, guess)
        x = x + dx/2
    else
        guess = newGuess
        x = x + dx
```

## APPENDIX C

### ANTAGONISTIC TIME PLOTS

Figures 18, 19, and 20 show optimal control, temperature, and force predicted by the linear and nonlinear models as functions of time for each reference signal. Plots are displayed for the optimal  $n = 2$  homogeneous bundle of  $d = 0.8$  mm and an arbitrary heterogeneous bundle of  $d_1 = 0.4$  mm and  $d_2 = 0.8$  mm.

### ACKNOWLEDGMENT

I would like to acknowledge Prof. Dr.-Ing. Heike Vallery. I greatly appreciate all of the guidance, support, and direction you provided over the last year. Thank you to Dr.ir. Ron van Ostayen and Prof.dr. Robert Babuska for your suggestions and direction as well.

Thank you to Court and Niyaz for all the moral support. Thank you to Wilrik for all the cafe trips and espressos. Most of all, thank you to my family for all of your help along the way.

### REFERENCES

- [1] C. S. Haines, M. D. Lima, N. Li, G. M. Spinks, J. Foroughi, J. D. Madden, S. H. Kim, S. Fang, M. Jung de Andrade, F. Göktepe *et al.*, “Artificial muscles from fishing line and sewing thread,” *science*, vol. 343, no. 6173, pp. 868–872, 2014.
- [2] A. Cherubini, G. Moretti, R. Vertechy, and M. Fontana, “Experimental characterization of thermally-activated artificial muscles based on coiled nylon fishing lines,” *AIP Advances*, vol. 5, no. 6, 2015.
- [3] S. H. Kim, M. D. Lima, M. E. Kozlov, C. S. Haines, G. M. Spinks, S. Aziz, C. Choi, H. J. Sim, X. Wang, H. Lu, D. Qian, J. D. W. Madden, R. H. Baughman, and S. J. Kim, “Harvesting temperature fluctuations as electrical energy using torsional and tensile polymer muscles,” *Energy and Environmental Science*, vol. 8, no. 11, pp. 3336–3344, 2015.
- [4] G. M. Spinks, “Stretchable artificial muscles from coiled polymer fibers,” *Journal of Materials Research*, vol. 31, no. 19, pp. 2917–2927, 2016.
- [5] M. C. Yip and G. Niemeyer, “High-performance robotic muscles from conductive nylon sewing thread,” in *Proceedings - IEEE International Conference on Robotics and Automation*, vol. 2015-June, 2015, pp. 2313–2318.
- [6] D. R. Higuera-Ruiz, H. P. Feigenbaum, and M. W. Shafer, “Moisture’s significant impact on twisted polymer actuation,” *Smart Materials and Structures*, vol. 29, no. 12, 2020.
- [7] M. Zinn, B. Roth, O. Khatib, and J. K. Salisbury, “A new actuation approach for human friendly robot design,” *The international journal of robotics research*, vol. 23, no. 4-5, pp. 379–398, 2004.
- [8] P. Daemi, M. Kamel, J. Gharibo, M. D. Naish, A. L. Trejos, and A. D. Price, “Control of twisted-coiled actuators via multi-dof pid,” in *Electroactive Polymer Actuators and Devices (EAPAD) XXIII*, vol. 11587. SPIE, 2021, pp. 28–39.
- [9] H. Song and Y. Hori, “Force control of twisted and coiled polymer actuators via active control of electrical heating and forced convective liquid cooling,” *Advanced Robotics*, vol. 32, no. 14, pp. 736–749, 2018.
- [10] X. Tang, Y. Liu, K. Li, W. Chen, and J. Zhao, “Finite element and analytical models for twisted and coiled actuator,” *Materials Research Express*, vol. 5, no. 1, 2018.
- [11] F. Karami and Y. Tadesse, “Modeling of tcp muscles for understanding actuation behavior,” in *ASME International Mechanical Engineering Congress and Exposition, Proceedings (IMECE)*, vol. 4A-2017, 2017.
- [12] A. Abbas and J. Zhao, “A physics based model for twisted and coiled actuator,” in *Proceedings - IEEE International Conference on Robotics and Automation*, 2017, pp. 6121–6126.
- [13] J. Van Der Weijde, B. Smit, M. Fritschi, C. Van De Kamp, and H. Vallery, “Self-sensing of deflection, force, and temperature for joule-heated twisted and coiled polymer muscles via electrical impedance,” *IEEE/ASME Transactions on Mechatronics*, vol. 22, no. 3, pp. 1268–1275, 2017.

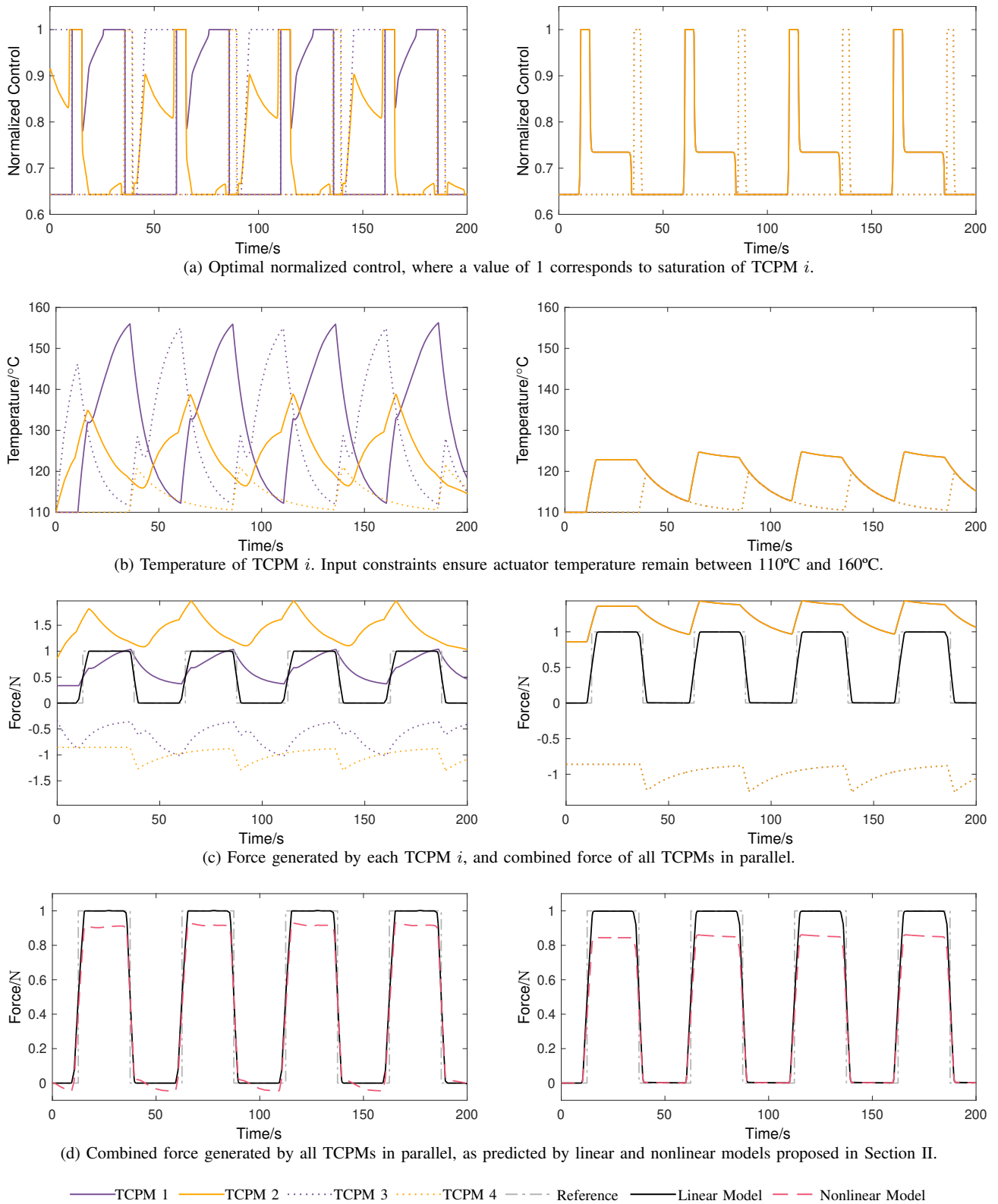


Fig. 18: (a) Optimal control, (b) temperature, and (c)(d) force as a function of time for  $n = 2$  antagonistic pairs of TCPMs in parallel. Left: response of the heterogeneous bundle with fiber diameters  $d_{1,3} = 0.4$  mm and  $d_{2,4} = 0.8$  mm. Right: response of the homogeneous bundle with optimal fiber diameter  $d = 0.8$  mm which minimizes tracking performance.

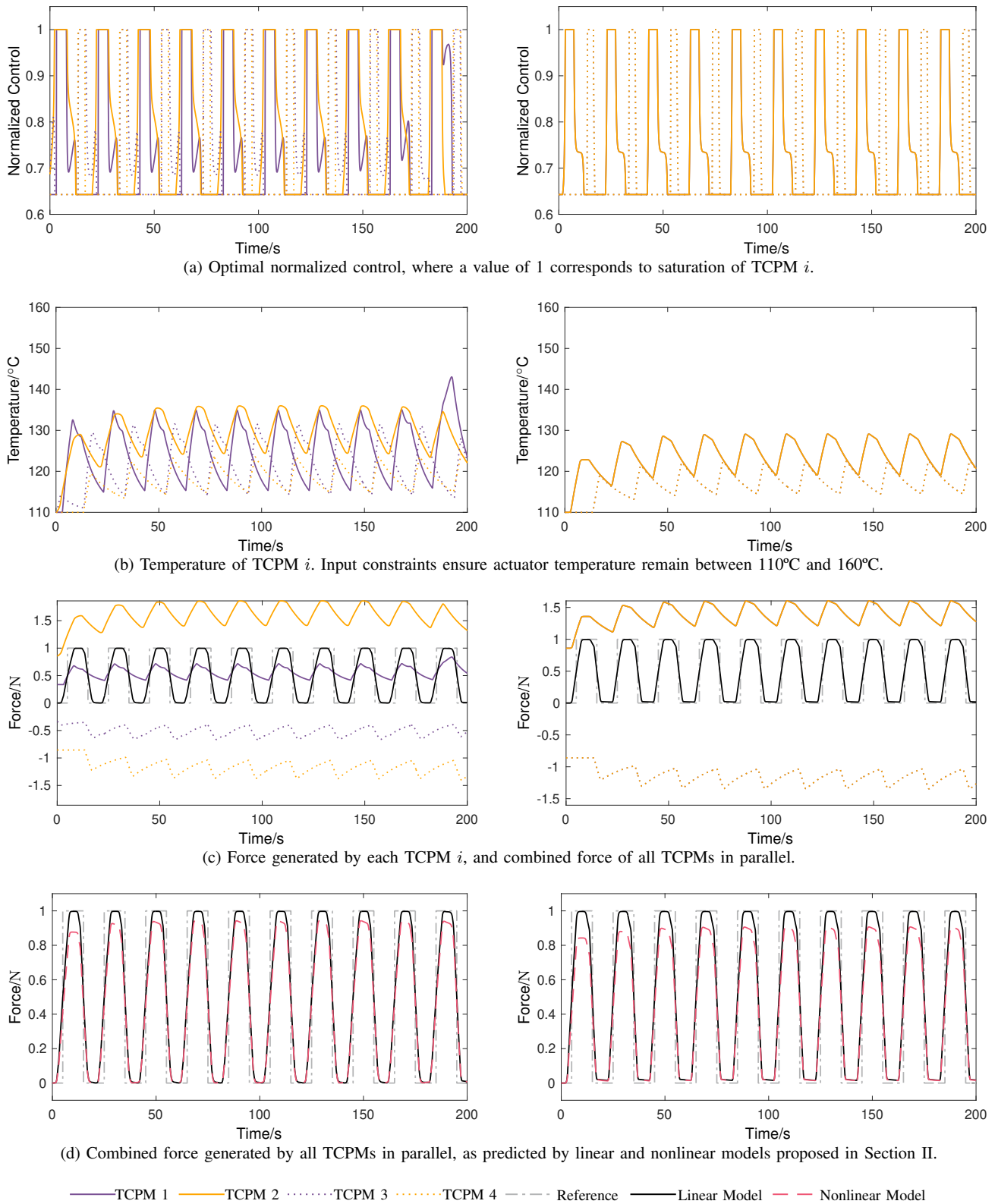


Fig. 19: (a) Optimal control, (b) temperature, and (c)(d) force as a function of time for  $n = 2$  antagonistic pairs of TCPMs in parallel. Left: response of the heterogeneous bundle with fiber diameters  $d_{1,3} = 0.4$  mm and  $d_{2,4} = 0.8$  mm. Right: response of the homogeneous bundle with optimal fiber diameter  $d = 0.8$  mm which minimizes tracking performance.

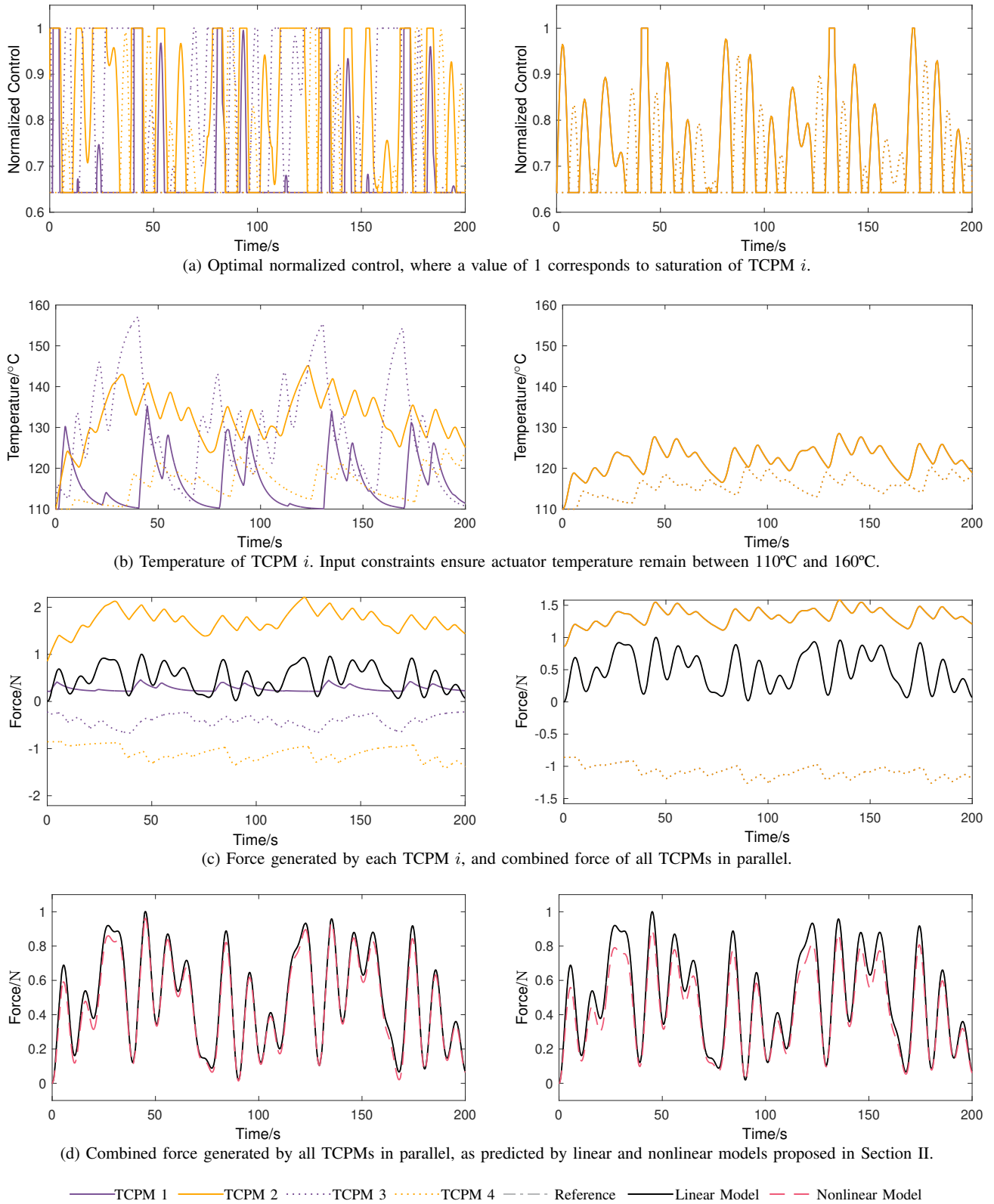


Fig. 20: (a) Optimal control, (b) temperature, and (c)(d) force as a function of time for  $n = 2$  antagonistic pairs of TCPMs in parallel. Left: response of the heterogeneous bundle with fiber diameters  $d_{1,3} = 0.4$  mm and  $d_{2,4} = 0.8$  mm. Right: response of the homogeneous bundle with optimal fiber diameter  $d = 0.8$  mm which minimizes tracking performance.

- [14] K. Masuya, S. Ono, K. Takagi, and K. Tahara, "Modeling framework for macroscopic dynamics of twisted and coiled polymer actuator driven by joule heating focusing on energy and convective heat transfer," *Sensors and Actuators, A: Physical*, vol. 267, pp. 443–454, 2017.
- [15] V. Giovinco, P. Kotak, V. Cichella, C. Maletta, and C. Lamuta, "Dynamic model for the tensile actuation of thermally and electro-thermally actuated twisted and coiled artificial muscles (teams)," *Smart Materials and Structures*, vol. 29, no. 2, 2020.
- [16] J. Van Der Weijde, H. Vallery, and R. Babuška, "Closed-loop control through self-sensing of a joule-heated twisted and coiled polymer muscle," *Soft Robotics*, vol. 6, no. 5, pp. 621–630, 2019.
- [17] Y. . Huang, W. . Lee, Y. . Chuang, W. Cao, F. Yang, and S. Lee, "Time-dependent deformation of artificial muscles based on nylon 6," *Materials Science and Engineering C*, vol. 98, pp. 445–451, 2019.
- [18] C. Wu and W. Zheng, "A modeling of twisted and coiled polymer artificial muscles based on elastic rod theory," *Actuators*, vol. 9, no. 2, 2020.
- [19] F. Karami, L. Wu, and Y. Tadesse, "Modeling of one-ply and two-ply twisted and coiled polymer artificial muscles," *IEEE/ASME Transactions on Mechatronics*, vol. 26, no. 1, pp. 300–310, 2021.
- [20] S. Aziz, S. Naficy, J. Foroughi, H. R. Brown, and G. M. Spinks, "Controlled and scalable torsional actuation of twisted nylon 6 fiber," *Journal of Polymer Science Part B: Polymer Physics*, vol. 54, no. 13, pp. 1278–1286, 2016.
- [21] D. R. Higuera-Ruiz, C. J. Center, H. P. Feigenbaum, A. M. Swartz, and M. W. Shafer, "Finite element analysis of straight twisted polymer actuators using precursor properties," *Smart Materials and Structures*, vol. 30, no. 2, 2021.
- [22] Q. Yang and G. Li, "A top-down multi-scale modeling for actuation response of polymeric artificial muscles," *Journal of the Mechanics and Physics of Solids*, vol. 92, pp. 237–259, 2016.
- [23] J. Hauser, "Berechnung der oberflächenbelastung von widerstandsheizelementen bei freier konvektion," *Elektrowärme Int.*, vol. 45, no. B2, pp. 82–87, 1985.
- [24] R. Rajput, *A textbook of electrical engineering materials*. Firewall Media, 2004.
- [25] C. Lamuta, S. Messelot, and S. Tawfick, "Theory of the tensile actuation of fiber reinforced coiled muscles," *Smart Materials and Structures*, vol. 27, no. 5, 2018.
- [26] S. Sharafi and G. Li, "A multiscale approach for modeling actuation response of polymeric artificial muscles," *Soft matter*, vol. 11, no. 19, pp. 3833–3843, 2015.
- [27] R. B. Pipes and P. Hubert, "Helical carbon nanotube arrays: mechanical properties," *Composites Science and Technology*, vol. 62, no. 3, pp. 419–428, 2002.
- [28] S.-M. An, J. Ryu, M. Cho, and K.-J. Cho, "Engineering design framework for a shape memory alloy coil spring actuator using a static two-state model," *Smart Materials and Structures*, vol. 21, no. 5, p. 055009, 2012.
- [29] J. Sweeney and I. M. Ward, *Mechanical Properties of Solid Polymers*. John Wiley & Sons, 2012.
- [30] A. Ross, "Cable kinking analysis and prevention," *American Society of Mechanical Engineers*, 1977.
- [31] "Solving boundary value problems," , MathWorks, Tech. Rep. r2022a, jun 2022.
- [32] W. Leung, K. Ho, and C. Choy, "Mechanical relaxations and moduli of oriented nylon 66 and nylon 6," *Journal of Polymer Science: Polymer Physics Edition*, vol. 22, no. 7, pp. 1173–1191, 1984.
- [33] V. Wasan, "Sag method for the determination of coefficient of linear thermal expansion of carbon fibres," *Carbon*, vol. 17, no. 1, pp. 55–58, 1979.
- [34] C. Choy, F. Chen, and K. Young, "Negative thermal expansion in oriented crystalline polymers," *Journal of Polymer Science: Polymer Physics Edition*, vol. 19, no. 2, pp. 335–352, 1981.
- [35] L. W. McKeen, *The effect of temperature and other factors on plastics and elastomers*. William Andrew, 2014.
- [36] W. Chen, Y. Zhang, Q. Gao, J. Liu, L. Wang, and J. Xu, "A fabrication device producing twisted and coiled polymer actuators for use in soft robots," in *2019 IEEE 9th Annual International Conference on CYBER Technology in Automation, Control, and Intelligent Systems (CYBER)*. IEEE, 2019, pp. 734–739.
- [37] L. Saharan and Y. Tadesse, "Fabrication parameters and performance relationship of twisted and coiled polymer muscles," in *ASME International Mechanical Engineering Congress and Exposition*, vol. 50688. American Society of Mechanical Engineers, 2016, p. V014T11A028.